Seismic Risk at Urban Scale:

The Role of Site Response Analysis

Raffaele De Risi[1], Augusto Penna[2], and Armando Lucio Simonelli[3]

[1] Department of Civil Engineering, Queen's Building, University Walk, University of Bristol, BS8 1TR, Bristol, UK; E-mail: raffaele.derisi@bristol.ac.uk

[2] Department of Engineering, University of Sannio, Piazza Roma 21, 82100 Benevento, Italy; E-mail: apenna@unisannio.it

[3] Department of Engineering, University of Sannio, Piazza Roma 21, 82100 Benevento, Italy; E-mail: alsimone@unisannio.it

Submitted to:

Soil Dynamics and Earthquake Engineering

Corresponding author:

Raffaele De Risi

E-mai: raffaele.derisi@bristol.ac.uk

Abstract

A refined seismic risk assessment at urban level is fundamental to identify the most correct risk mitigation policies, both in short and long terms. To date, seismic risk assessment frameworks at regional level consider the site response by means of simplified geotechnical analyses. This study investigates how different procedures of site response analysis influence the risk quantification at urban scale. Simplified and refined analyses are computed and compared for the urban area of Benvento, Italy. For the risk assessment, a stochastic scenario-based approach is adopted, and the risk is quantified in terms of direct losses incurred by the portfolio of buildings in Benevento for a specific historical seismic event, i.e. the 1980 M_w6.9 Irpinia earthquake. It is demonstrated that simplified approaches for the site response analysis can be unreliable, and the knowledge of the exposure behavior is a key element to appraise the importance of the site response. Finally, a risk-based microzonation is proposed, according to the new philosophy of risk-based hazard maps that may be adopted to achieve an optimal development of the urban areas, ensuring an equal distribution of the risk among the population.

Keywords: shear wave velocity; mono-dimensional propagation; ground motion prediction equations; shakemaps; fragility curves; microzonation.

1 INTRODUCTION

Fast-growing city regions are the center of the major economic activities of modern societies and are the drivers of the national economies. Given the high exposure concentration, and the high level of complexity that increases the overall vulnerability, urban areas are characterized by potentially high risk to natural hazards and can be highly affected by unexpected and unforeseen natural catastrophes. In seismic prone regions, earthquakes are among the most significant hazards that can threat the urban built environment and cause potential human and economic losses. Urban seismic risk concerns spatially distributed portfolio of structures and/or infrastructures (Gavarini, 2001) and is assessed by integrating spatially correlated hazard scenarios (Weatherill et al., 2015), seismic vulnerability models of the exposed portfolio of structures and/or infrastructures (Sousa et al., 2018), and the economic value of the exposed asset of interest (Miano et al., 2015). Seismic risk assessment at urban scale is of paramount importance for two reasons. First, it provides a quantification of the socio-economic impact of potential future earthquakes on densely-populated areas (Smerzini and Pitilakis, 2018), offering key information to relevant stakeholders such as engineers, insurers, reinsurers, brokers, capital market investors, and corporations. Second, it helps local and national governmental institutions (e.g., the civil protection) in planning effective policies of risk mitigation during peacetime (Cosenza et al., 2018) and improving the preparedness that is necessary during the emergency in the aftermath of a seismic event (De Risi et al., 2018). Therefore, it is essential to have robust and reliable probabilistic quantification algorithms and tools for the seismic risk assessment at urban level (Sahin et al., 2016; Kotha et al., 2018).

One of the most adopted methodologies for the assessment of the seismic risk at urban level consists in the generation of earthquake scenarios that can be deterministic (Ansal et al. 2009) or fully probabilistic (Goda and De Risi, 2017). An earthquake scenario provides the risk quantification, for a portfolio of exposed assets, associated with a specific earthquake event

(i.e., given magnitude and source characteristics). For example, in the field of catastrophe risk modelling, the seismic risk at regional level is computed creating earthquake scenarios for each event defined in a stochastic earthquake catalogue (Atkinson and Goda, 2013), adopting a modular nested framework according to the performance-based earthquake engineering approach (PBEE, Cornell and Krawinkler, 2000). This modular structure is very effective since it allows (a) to propagate the uncertainties associated with all the risk components (i.e., hazard, vulnerability and exposure), and (b) to implement specific physics-based model components such as source, path, and local site response effects (Bazzurro and Cornell, 2004; Ansal et al. 2010, Goda et al., 2017; Goda and De Risi, 2018; Smerzini and Pitilakis, 2018).

As demonstrated by recent earthquakes, local site response plays a crucial role in the extent and nature of the damage patterns observed for different structural systems at urban scale (Maugeri et al., 2011; Assimaki et al., 2012; Sextos et al., 2018). Physical damage is further exacerbated if also ground failures (e.g., landslides and liquefaction) occur (Esposito et al., 2000; Bray et al., 2012; Franke et al., 2018). It is therefore very important to take into account site effects in the seismic risk assessment at urban level. Such site response effects can be introduced in the general risk framework by means of a microzonation analysis, i.e., the study of the variation imposed by the local geotechnical and topographic conditions to the earthquake frequency and amplitude contents.

Microzonation analyses can be carried out with an increasing level of sophistication (ISSMGE, 1999): Level-1, general zonation; Level-2, detailed zonation; Level-3, rigorous zonation. Level-1 in general does not require any numerical quantification and consists mainly in the realization of detailed geological maps and sections. On the contrary, Level-2 microzonation can be carried out through simplified approaches using soil classification based on detailed geotechnical tests (Stewart et al., 2014) and Level-3 microzonation can be carried out by performing mono-dimensional (1D), bi-dimensional (2D) or tri-dimensional (3D) wave

93 propagation analyses (Semblat, 2010; Smerzini et al., 2011) in linear, linear equivalent, or non-
94 linear regime (Kim et al., 2016; Falcone et al., 2018). For Level-2 approaches, empirical
95 amplification factors can be calculated either with microtremor analyses (e.g., Nakamura,
96 1989) or by defining soil categories (Baturay and Stewart, 2003; Stewart et al., 2003) that can
97 be identified either on the basis of the shear wave velocity in the uppermost thirty meters of
98 soil column (V_{S30}, Foti et al., 2018) or, alternatively, on the basis of proxy variables, such as
99 local topography or geo-lithology (Ohta and Goto, 1978; Allen and Wald, 2009). For Level-3
100 approaches, detailed stratigraphic data are needed as well as numerous laboratory tests, such
101 as resonant column or torsional shear (Vardanega and Boltom, 2013). Therefore, given the
102 potential lack of high-quality/high-resolution data, and given the high sophistication of the
103 required numerical models and high computational costs, it is not always possible to perform
104 more sophisticated analyses, especially if the geographical area of interest has a large
105 extension.

106 In the literature there are several studies implementing site response to obtain the
107 seismic microzonation at urban level (Pergalani et al., 2006; Grasso and Maugeri, 2009; Lanzo
108 et al., 2011; Panzera et al., 2011; Grasso and Maugeri, 2014; Smerzini et al., 2017) but only
109 few studies investigated thoroughly what is the role of site response on risk assessment at urban
110 scale (Dolce et al., 2003; Romeo and Bisiccia, 2006; Pergalami et al., 2008; Sahin et al., 2016;
111 Smerzini and Pitilakis, 2018). Dolce et al. (2003) demonstrated that including the
112 microzonation in the scenario-based damage assessment can lead to a dramatic shift from lower
113 to severe damage states. Romeo and Bisiccia (2006) and Pergalani et al. (2008) presented
114 simplified microzonation approaches that can help with the identification of areas of the urban
115 built environment at higher risk, emphasizing the necessity of a risk-oriented microzonation.
116 Sahin et al. (2016) proposed an integrated earthquake simulation system to study, in dynamic
117 regime, the seismic behavior of the virtual twin of a city composed by the subsoil and the

buildings that are schematized as linear multi degree of freedom systems; the proposed framework includes site amplification through 1D propagation analyses. Although this study is very advanced, only few records of a single event are adopted, and no damage is identified at city level. Finally, Smerzini and Pitilakis (2018) presented a 3D physic-based numerical simulation of the earthquake that accounts for fault rupture, propagation path and complex geological conditions. They considered the vulnerability only for reinforced-concrete buildings in their case-study area by means of a combination of the capacity spectrum method (Freeman, 2004) and fragility curves (Porter et al., 2007), and represented the risk with city-level maps in terms of expected damage ratio, i.e., the expected cost of repair normalized with respect to the reconstruction cost.

Building upon the previous literature, this paper presents three new insights about the role of site response analysis in the urban seismic risk. First, the influence of the quality of available geotechnical data characterizing the ground underneath an urban area is explored; more specifically, risk profiles obtained neglecting the site response, or considering it using open-access soil classification data, are compared with the risk profile obtained in the case of detailed geotechnical knowledge. Second, the influence of simplified and more refined linear and non-linear mono-dimensional site response analyses on the risk assessment, is investigated. Finally, a risk break-down is proposed to assess which component of the built environment (i.e. which structural typology) is more at risk and why; moreover, a risk-oriented microzonation is proposed as first step towards risk-target hazard maps (Silva et al., 2016). The study is conducted by adopting the stochastic earthquake scenario method, considering as reference event the magnitude M_W-6.9 1980 Irpinia earthquake (Ameri et al., 2011).

As case study, the Italian city of Benevento is selected. Benevento is located 50 km NE of Naples and 200 km SE of Rome; it was frequently stricken by severe seismic events (e.g., 1456, 1688, 1702 and 1732, see Iannaccone et al., 1995), several of which induced both

143 structural and geotechnical failures (Martino et al., 2014). Only an official Level-1 study was
144 commissioned by the local municipality government in the first decade of the 2000s and is
145 freely available on the municipality website (CDB, 2018); from a scientific point of view, many
146 advanced microzonation studies have already been performed (Improta et al., 2005; Santucci
147 de Magistris et al., 2005; Di Giulio et al., 2008) and reliable geotechnical data are available.
148 Taking advantage of the available data, according to the Guideline for Microzonation proposed
149 by the Italian Civil Protection (SMWG, 2015), and in line with the work currently carried out
150 by the Italian Center for Seismic Microzonation, a new microzonation analysis is carried out
151 for a large part of the urban area, performing both linear and non-linear mono-dimensional site
152 response analyses using both components of 150 natural records (i.e., 300 accelerograms) from
153 the Italian database ITACA (Luzi et al., 2017). Moreover, a new GIS (Geographical
154 Information System) database of masonry and reinforced concrete buildings in Benevento is
155 compiled; such a database contains relevant information such as the geometric footprint, the
156 structural typology, the number of storeys, the total height, and other relevant information
157 necessary for the assessment of the total economic value. Structural vulnerability of the
158 buildings is modelled adopting seismic fragility curves that are appropriate for European
159 reinforced concrete buildings (Rossetto and Elnashai, 2003) and for Italian masonry buildings
160 (Rota et al. 2008).

161 In the following, after the presentation of the probabilistic loss estimation framework
162 that accounts for site response (Section 2), the case study is presented (Section 3), results are
163 shown and commented (Section 4), main conclusion are drawn, and limitation and potential
164 developments of the study are discussed (Section 5).

165

166 ## 2 RISK ASSESSMENT FRAMEWORK

167 A generic equation for probabilistic urban seismic risk assessment can be expressed as:

$$P(L \geq l) = \sum_{i=1}^{N_B} \iint P_i(L \geq l|ds) \cdot f_{i,DS|IM}(ds|im) \cdot f_i(im) \cdot |\mathrm{d}ds| \cdot |\mathrm{d}im| \quad (1)$$

where $P(L \geq l)$ is the probability that the earthquake loss L for a portfolio of buildings exceeds a specific threshold l. The variables *IM* and *DS* are the earthquake intensity measure and the structural damage state, respectively. Example of *IM* are the peak ground acceleration (PGA) or the spectral acceleration $S_a(T)$ for a given vibration period (T). The term $f_i(im)$ represents the probability density function of *IM* and can be calculated either by a probabilistic seismic hazard analysis (Cornell, 1968; McGuire, 2004) or by a stochastic earthquake scenario analysis (De Risi and Goda, 2016). $f_{i,DS|IM}(ds|im)$ is the seismic fragility function for the i^{th} building, that is the probability of attaining a given damage state *DS* for a given intensity measure *IM*. $P_i(L \geq l|ds)$ is the earthquake loss function and can be represented by the damage-loss function (generally a range of damage ratios *DR* for given *DS*) and the building cost model; a damage ratio is defined as a fraction of the total building replacement cost. Finally, N_B is the number of buildings in the considered urban area. In Equation 1, *IM* and *DS* are presented as continuous random variables; from a practical point of view they are generally evaluated in a discrete manner, and therefore the integral can be replaced by a summation. In this study, a standard Monte Carlo simulation framework is used to solve Equation 1.

Figure 1 shows different steps of the computational procedure adopted for carrying out the probabilistic seismic risk assessment based on stochastic earthquake scenarios. The first step is the identification of the exposure (i.e., the portfolio of buildings at risk in a selected urban area, e.g., Benevento) and of the seismic sources of interest (Figure 1a). For the case of a scenario approach, the seismic source is completely defined by the geometry of the fault (or fault system) that was activated during a specific historical event of a given magnitude. The second step is the definition of an earthquake shaking model by means of which it is possible to generate fields of seismic intensity measures at urban scale (e.g., a shakemap, Figure 1b)

and therefore it is possible to simulate *IMs* at each building location ($f_i(im)$, Figure 1c). For this step, intensity measures are calculated adopting suitable ground motion prediction equations (GMPEs, Douglas, 2003) together with suitable spatial correlation and spectral cross-correlation models (Weatherill et al., 2014). The third step consists in calculating, for each building, the probability of attaining a specific damage state ($f_{i,DS|IM}(ds|im)$) for each simulated intensity measure (Figure 1d). This probability is obtained as the difference of the estimated exceedance probabilities for two adjacent damage states, i.e. the difference between the probability values of two adjacent fragility curves (see the colored bar in Figure 1d obtained for a given *im*). Subsequently, a random number (between 0 and 1) is sampled from a standard uniform distribution and is compared with the damage state probabilities; this number will determine the realized damage state for the i^{th} structure for the simulated earthquake event (e.g., the circle in Figure 1d shows that, for the specific *im*, a ds4 is attained). The fourth step consists in associating to each realized damage state a value that is sampled from a range of damage ratios (Figure 1e). As in the previous case, the sampling can be carried out using a uniform distribution. Finally, multiplying the sampled damage ratio by the total cost of the building, the earthquake loss can be calculated (i.e., $P_i(L \geq l|ds)$). Repeating this procedure for all the simulated *im* values and for all the buildings, it will be possible to obtain a loss curve (Figure 1f), showing the probability that a given loss for the entire portfolio of structure is exceeded.

It is important to clarify that the risk assessment procedure adopted by insurance and reinsurance companies is different from the classic one proposed herein since damage functions (i.e., expected loss as function of the intensity measure) are adopted instead of the combination of fragility functions and loss model.

2.1 The shakemap model

A stochastic simulation-based procedure is herein adopted to estimate seismic *IM*s for each building of the considered portfolio of structures (i.e. a shakemap). This approach is largely adopted to predict *IM*s probabilistically due to a specific earthquake scenario (e.g., Wald et al. 2006). Such *IM*s need to be spatially correlated, so that the distribution of intensity measures is not completely random but is constrained on the inter-distances between the sites (Goda and Hong, 2008). Moreover, *IM*s should be efficient, i.e., they should be highly correlated with *DS* for each specific building. For example, for a mid-rise reinforced concrete building, it was demonstrated that the spectral acceleration corresponding to the first vibration period is more efficient than the peak ground acceleration. Therefore, in the same simulation several *IM*s (e.g., PGA, Sa(T), etc.) need to be simulated considering the correlation of the spectral accelerations at different vibration periods (Baker and Cornell, 2006). The incorporation of the latter aspect is significant because seismic effects on structural systems having similar characteristics (e.g., material, number of storeys, etc.) are more correlated than those with different characteristics; this feature allows to observe concentrated seismic losses for a particular class of structures for a given scenario.

The shakemap simulation is performed assuming that *IM*s (in the following the bold $\boldsymbol{IM}$ will be used to represent the vector format) are distributed according to a joint lognormal distribution, with central values $\overline{\boldsymbol{IM}}$ computed by a GMPE and covariance matrix $\boldsymbol{\Sigma}$ calculated with a correlation model on the bases of the GMPE's intra-event standard deviations (Weatherill et al., 2015):

$$log(\boldsymbol{IM}) \sim N(log(\overline{\boldsymbol{IM}}), \boldsymbol{\Sigma}) \quad (2)$$

The general form of the covariance matrix $\boldsymbol{\Sigma}$ is:

$$\boldsymbol{\Sigma} = \begin{bmatrix} \boldsymbol{\Sigma_{IM1}} & \cdots & \boldsymbol{\Sigma_{IMn,IMi}} \\ \vdots & \ddots & \vdots \\ \boldsymbol{\Sigma_{IMn,IMi}} & \cdots & \boldsymbol{\Sigma_{IMn}} \end{bmatrix} \quad (3)$$

where the matrixes $\boldsymbol{\Sigma_{IMi}}$ represent the covariance matrixes of the single considered *IM*s (e.g., PGA, $S_a(T)$, etc.) and the matrixes $\boldsymbol{\Sigma_{IMi,IMj}}$ are the cross-covariance matrixes between two *IM*s. The general covariance matrix ($\boldsymbol{\Sigma_{IMi}}$) is obtained multiplying the square of the intra-event standard error ($\sigma_{I,IMi}$) of the selected GMPE by the spatial correlation matrix:

$$\boldsymbol{\Sigma_{IMi}} = \sigma^2_{I,IMi} \begin{bmatrix} 1 & \cdots & \rho_{a,b}(R_{a,b}) \\ \vdots & \ddots & \vdots \\ \rho_{b,a}(R_{b,a}) & \cdots & 1 \end{bmatrix} \quad (4)$$

where the term of the correlation matrix $\rho_{a,b}(R_{a,b})$ is function of the inter-distance $(R_{a,b})$ between two general sites *a* and *b*. Correlation coefficients can be calculated adopting one of the many formulations available in the literature (e.g., Goda and Atkinson 2010; Esposito and Iervolino 2011, 2012).

The general cross-covariance matrix ($\boldsymbol{\Sigma_{IMi,IMj}}$) is obtained by multiplying the correlation coefficient for different *IM*s ($\rho_{IMi,IMj}$) by the Cholesky factorization of the matrix $\boldsymbol{\Sigma_{IMi}}$ and by the transpose of the Cholesky factorization of the matrix $\boldsymbol{\Sigma_{IMj}}$ (Oliver, 2003). As in the previous case, several equations for calculating cross-correlation coefficients are available in literature (Baker and Cornell, 2006; Goda and Atkinson, 2009; Cimellaro, 2013).

Structuring the covariance matrix in this manner it is possible to take into account not only the spatial correlation between a single typology of intensity measure but also the spatial cross-correlation between different typologies of intensity measures.

2.2 The role of the site response

The site response can be implemented in the hazard term ($f_i(im)$) of the Equation 1. More specifically, the intensity measure values at the ground surface ($IM_{surface}$) are obtained multiplying the intensity measure values at the engineering bedrock (IM_{rock}) by a period-dependent site response factor ($SRF(T)$):

$$IM_{surface} = IM_{rock} \cdot SRF(T)$$
$$log(IM_{surface}) = log(IM_{rock}) + log[SRF(T)] \quad (5)$$

Many of the available GMPEs provide values of *SRF(T)* based on simplified (generally V_{S30}-based) classification of the soil (e.g., Iervolino, 2016). On the other hand, *SRF(T)* can be assessed by carrying out more refined wave propagation analyses. Such analyses require refined geotechnical data and can be performed either using the random vibration theory approaches (Kottke and Rathje, 2013; Stanko et al., 2019) or selecting a proper suite of ground motions as input. The adopted set of ground motions should be, ideally, hazard consistent (Convertito et al., 2009; Iervolino et al., 2010), or, at least, should be compatible with the geophysical framework of the area of interest (earthquakes corresponding to a specific faulting style, and of magnitude belonging to a specific range). In the following, the seismic risk assessment is evaluated considering different approaches for calculating *SRF(T)*.

3 CASE STUDY

This study focuses on the main urbanized area of Benevento, a city in the Southern Italy with a population of about 60,000 people, that is the most important city in the Sannio area in Campania region. The Sannio area is situated in the northern part of the Southern Apennine seismic belt, one of the most seismic-prone area of Italy, as demonstrated by the high number of earthquakes that occurred in this area (Rovida et al., 2016, Figure 2a). More specifically, the case-study covers nearly 9 km^2 around the Benevento old-town neighborhood and is located at

276 the confluence of Calore and Sabato rivers spanning from 118 m to 338 m above the sea level
277 (Figure 2b). The more ancient part of the town is located at the top of the hill formed by fluvial
278 deposits and alluvial terraces, meanwhile the more recent part of the town is in the alluvial
279 valley of the rivers, as shown by the regional geologic map (GRC, 2018; Figure 2c) and geo-
280 lithological map (GN, 2018; Figure 2d). The two rivers, alternating deposition and erosion
281 cycles, led to a heterogeneous geo-lithological structure formed of alternating alluvial and
282 palustrine layers, with large areas of soft-soil conditions (Di Giulio et al., 2008). Therefore, a
283 proper evaluation of the site effects is crucial for the seismic risk assessment of the city. A
284 further representation of the case study is shown in Figure 3, where characteristics of the
285 bedrock are presented (Figure 3a) and three geological sections are also shown (Figures 3b, 3c,
286 and 3d). More specifically, the black contour and the raster in Figure 3a represent the depth of
287 the bedrock and the value of the shear wave velocity at the bedrock level, respectively.
288
289 **3.1 Available geotechnical data**
290 Two main data resources are adopted for the geotechnical modelling of the Benevento's
291 subsoil. The first dataset contains open-access data available at the U.S. Geological Survey
292 (USGS) Global VS30 Server (USGS, 2017). Specifically, data consist in maps of V_{S30} (Figure
293 4a) obtained as function of the topographic slope (Wald and Allen, 2007; Allen and Wald,
294 2009) and have a resolution of 30 arcseconds (i.e., about 900 meters). The second dataset
295 consists of 263 site investigations (black dots in Figure 4b) spanning across the entire case-
296 study area; among those investigations, 30 Down-Holes, and 70 Standard Penetration Tests
297 (SPT) are available. The depths of the tests span from 15 m and 50 m. Moreover, the 30 Down-
298 Holes were used in combination with nearby SPT to calibrate a N_{SPT}-V_S regression for the
299 specific case-study area, that allowed to obtain values of shear wave velocities also where only
300 SPT were available. This is a consolidate practice in the field of seismic geotechnical

engineering (Brandenberg et al. 2010; Wair et al., 2012). More details on these specific regressions are available in Penna (2005). These tests allowed to obtain a refined geotechnical model of the city, consisting of a lattice of 6,156 50-m × 50-m squared grid cells. Each cell contains values of shear wave velocities (V_S) for each 1-meter layer from the ground level to the bedrock; such V_S values were obtained by means of an Ordinary Kriging geostatistical analysis (Chilès and Delfiner, 2012) that is detailed in (Penna, 2005). Figure 4b shows the map of V_{S30} obtained on the basis of these more refined data. From the analysis of the more detailed data it emerged that most of the subsoil is made of Pliocene clay (spanning from tens to hundreds of meters below the ground level) covered by mixed alluvial deposits. Such layer of Pliocene clay is herein used as bedrock for the mono-dimensional propagation analyses. The adopted information about the bedrock are extensively discussed in several studies (Improta et al., 2005; Santucci de Magistris et al., 2005; Di Giulio et al., 2008). Figure 3a shows the contours of the depth of the top of layer of Pliocene clay, which is found at more than 20 m in the Northern part of the town, while in the Southern area the depth ranges between 5 and 20 m. Due to the variable lithostatic stress state, the Pliocene clay is characterized by a different shear wave velocity, depending on the depth of the top of the formation. Specifically, V_S is equal to about 550 m/s for depths between 5 and 15 m, while it increases up to 650 m/s where the top of the formation is between 15 and 30 m deep, and reaches values as high as 800 m/s for depths larger than 30 m.

Figures 4c and 4d show the soil classification according to Eurocode 8 (EN 1998-1, 2003), that classifies the soil in five main classes (i.e., A, B, C, D, E) based on the V_{S30} and the thickness of the soil profile; it is worth noting that this zonation is quite rough, since only two categories are identified using the USGS data (soil B and C) and only three categories using the more refined data (B, C, and E). This is a critical aspect, and only recently several studies were conducted to propose more refined soil classifications (Ciancimino et al., 2018).

The detailed geotechnical database provides also with the mechanical properties of the soils obtained as a combination of bespoke laboratory investigations (i.e., resonant column-torsional shear tests, direct shear tests and triaxial compression test with local strain measurements were performed for undisturbed samples of soil) and literature data available on comparable soils. Table 1 lists the mechanical properties associated with all the geotechnical units composing Benevento's subsoil that are used for the non-linear mono-dimensional propagation analysis. Specifically, the non-linear stiffness degradation follows the Ramberg-Osgood (1943) model:

$$\gamma\left(\frac{G}{G_0}\right) = \left[\frac{1-\frac{G}{G_0}}{C\cdot\left(\frac{G}{G_0}\right)^R}\right]^{\frac{1}{R-1}} \quad (6)$$

where γ is the shear strain, G is the current soil shear modulus that decreases with γ (i.e., softening), G_0 is the initial soil shear modulus, and C and R are the Ramberg-Osgood parameters listed in Table 1.

On the contrary, the damping ratio (ξ) increases with the strain level γ, and it is obtained as suggested by Santucci de Magistris et al. (2004):

$$\xi(\gamma) = \xi_0 + \frac{2}{\pi}\cdot\frac{R-1}{R+1}\cdot\left(1-\frac{G(\gamma)}{G_0}\right) \quad (7)$$

where ξ_0 is the initial damping ratio listed in Table 1. Figure 5 shows the non-linear soil behavior in terms of G/G_0-γ and ξ- γ obtained by means of Equations 6 and 7, respectively.

3.2 Considered site-response cases

Based on the available geotechnical data, five different cases are considered to study the role of the seismic site response in terms of effects induced on the risk at urban scale:

1. *SRF(T)* equal to 1 for the entire urban area; i.e., the site response effects are neglected;
2. *SRF(T)* calculated according to the GMPE as function of the USGS V_{S30} values;
3. *SRF(T)* calculated according to the GMPE as function of the V_{S30} values obtained on the basis of the site investigations;
4. *SRF(T)* calculated on the basis of a linear mono-dimensional propagation analysis for each cell of the comprehensive geotechnical database;
5. *SRF(T)* calculated on the basis of an equivalent linear (in the following referred as non-linear) mono-dimensional propagation analysis for each cell of the comprehensive geotechnical database.

It is worth noting that according to the Guideline for Microzonation proposed by the Italian Civil Protection (SMWG, 2015), Case 1 together with the geological and geo-lithological maps is a Level-1 microzoning study; Cases 2 and 3 are Level-2 studies; Cases 4 and 5 are Level-3 studies.

Mono-dimensional propagation analyses are carried out by means of SHAKE91 (Idriss and Sun, 1992). Authors are aware that bi-dimensional or three-dimensional analyses can lead to different (potentially more accurate) estimations since they take into account also geometrical effects; on the other hand, SHAKE91 allows reasonable computational time for such an extended area, especially if the number of ground motions adopted as input is large (see Section 3.6). It is possible to modify the mono-dimensional results by means of aggravation factors (Chávez-García and Faccioli, 2000) that allow considering the potential heterogeneity of the geomorphic conditions (e.g., 2D or 3D effects; Makra et al., 2005; Psarropoulos et al., 2007; Gelagoti et al., 2010; 2012); unfortunately, the majority of the study focuses on ideal trapezoidal basins (Riga et al., 2016), and a relationship providing the aggravation factors for the application in real case studies is still missing. Therefore, this additional aspect is neglected in this study.

370

371 ### 3.3 The exposure model

372 The seismic risk at urban scale is herein assessed considering as exposed asset the portfolio of
373 buildings in the case study area (Figure 6a). Specifically, a GIS database of the buildings was
374 manually built taking advantage of the technical cartography of Campania region, the Italian
375 cadastral maps (AE, 2018), the freeware data available in the OpenStreet maps (OSM, 2018),
376 the most recent regional satellite imagery available from several on-line resources (e.g., Google
377 Maps, Bing Maps), and the maps of the built environment available at GN (2018).
378 In literature it has been shown that geo-database built on the basis of freeware data can be
379 unreliable for risk assessment (Sousa et al., 2017); therefore, to improve the reliability of the
380 new database, a meticulous cross-checking of remote data was performed, and a quick visual
381 inspection during site surveys was organized to identify and solve the most ambiguous cases.
382 Analyzing the collected data, it emerges that there is an equal distribution of reinforced
383 concrete and masonry buildings (Figure 6b). Almost 90% of buildings are residential (Figure
384 6c). The maximum number of storeys for masonry and reinforced concrete structures is less
385 than 5 and 9, respectively (Figure 6d). Finally, the maximum building height is less than 30 m
386 (Figure 6e).
387 The GIS database is also provided with real estate estimations obtained from the Italian
388 real estate observatory (OMI, 2018). The portfolio of buildings can be classified into five OMI
389 categories according to the area in which they are (Figure 6a): B1, old town in downtown; C1,
390 first class close to the downtown; D1, outskirts; B2, downtown; C2, second class close to the
391 downtown. The minimum and maximum values proposed by the OMI for these five classes are
392 shown in Table 2. The building cost model adopted in this research is also probabilistic.
393 Specifically, the minimum and the maximum values presented in Table 2 are adopted as the

extremes of uniform distributions from which is randomly sampled in the stochastic approach presented in Figure 1.

It is worth noting that, in this study, only direct losses related to structural damage are considered; loss of building contents, downtime, casualties, and human suffering due to seismic events are disregarded since they are difficult to quantify at urban scale and are beyond the scope of this paper.

3.4 The vulnerability and loss models

Once the exposed asset at risk is identified, the most appropriate vulnerability models can be selected. Generally, in a performance-based earthquake engineering approach, a generic vulnerability model consists in a group of fragility curves representing the probability of exceeding a given set of damage states for a given level of intensity measure associated with the expected strong motion (Porter et al., 2007). The more appropriate intensity measure to adopt depends by the considered structural system (e.g., reinforced concrete frames, masonry structures, steel concentric braced frames, etc.). For the considered portfolio of structures in Benevento, the best intensity measure possible is the spectral acceleration corresponding to the fundamental elastic vibration period (T_1). In fact, it was demonstrated that, for simple buildings, spectral acceleration corresponding to T_1 has both high efficiency and sufficiency (Ebrahimian et al., 2015). It is therefore important to be able to compute T_1 for all the buildings in the case-study portfolio.

Figure 7a shows, with continuous lines, a typical empirical relationship used to calculate T_1 as function of the building height (H), i.e., $T_1 = \alpha \times H^{3/4}$ (Calvi, 1999), with H expressed in meters and α equal to 0.05 and 0.075 for masonry and reinforced concrete structures, respectively. The values of vibration periods for the buildings in the case-study area are also presented on the same plot with square and circular markers for reinforced concrete and

masonry structures, respectively. Figure 7b shows the comparison between the previous empirical relationship with an alternative empirical relationship (i.e. $T_1^* = N/10$, where N is the number of storeys, Crowley and Pinho, 2008); the points are almost all aligned along the diagonal, i.e., the two estimations tend to coincide. Only for one-story buildings there is not coincidence since the second empirical relationship (i.e., the function in terms of N) does not work properly for churches and industrial buildings, that are typical one-story buildings in Benvento. The distribution of the period for reinforced concrete and masonry buildings is shown in Figure 7c. Masonry structures are generally very stiff, with vibration periods smaller than 0.5 seconds, meanwhile reinforced concrete structures are more deformable with vibration period up to 1 second.

Two groups of fragility curves are selected. For masonry structures the empirical fragility functions proposed by Rota et al. (2008) are adopted (Figure 8a). These fragilities were derived on the basis of post-earthquake survey data for the specific case of the Italian building portfolio of masonry structures; they have a lognormal functional form and are expressed in terms of PGA. The adoption of PGA is also coherent with the stiff nature of the case-study structures that is shown in Figure 7. Moreover, most of the fragility functions for masonry structures in literature are presented in terms of PGA (Rota et al., 2010). More specifically herein fragilities proposed by Rota et al. (2008) are aggregated in two major groups: (a) structures with $N \leq 2$ and (b) structures with $N > 2$.

For reinforced concrete structures, the empirical fragility curves proposed by Rossetto and Elnashai (2003) for the European portfolio of structures, are adopted (Figure 8b). Curves have an exponential functional form and are expressed in terms of $Sa(T_1)$.

The fragility functions for both reinforced concrete and masonry structures are defined for five damage states according to European Macro-seismic Scale (Grünthal, 1998): DS1, Slight damage; DS2, Light damage; DS3, Moderate damage; DS4, Extensive damage; DS5, Collapse.

As explained in Section 2, the loss model is a function of the damage state and is expressed in terms of intervals of damage ratio, i.e., fractions of the total building cost. Herein, the damage ratio intervals suggested by Rossetto and Elnashai (2003) are adopted: DS1, 0% to 10%; DS2, 10% to 40%; DS3, 40% to 70%; DS4, 70% to 90%; DS5, 90% to 100%. Figure 1e shows the graphical representations of such damage ratio intervals.

3.5 The earthquake scenario

Irpinia Earthquake is a Mw 6.9 seismic event that struck the South of Italy on 1980, November 23. It caused structural damage in tens of municipalities within a radius of 200km from the epicenter, and it killed more than 3,000 people (Bernard and Zollo, 1989). To date, it is the strongest earthquake ever instrumentally recorded in Italy. It is characterized by a normal faulting style, and it involved the activation of three different faults that are nowadays relatively well known (Lancieri and Zollo, 2009) and are represented in Figure 9a.

To obtain shake maps representative of the Irpinia seismic event, in this study the GMPE proposed by Bindi et al. (2011) is adopted since it is the most suitable for the Italian territory. This GMPE is also provided with magnitude-independent *SRF(T)* values that allow to consider the site conditions. Figure 9b shows the PGA values recorded by accelerometric stations that are located on soil B; on the same plot the Bindi et al.'s GMPE is also shown. The PGA values recorded during the event are within the plus/minus one standard deviation interval of the GMPE.

The shakemaps generated within this study, as explained in Section 2.1, take into account the spatial correlation and the cross-correlation between spectral accelerations at different vibration periods. The spatial correlation models proposed by Esposito and Iervolino (2012) are adopted (Figure 10a), since they are tailored for the Bindi et al., GMPE.

$$\rho_{a,b}(R_{a,b}) = exp\left(-3 \cdot \frac{R_{a,b}}{b(T)}\right) \quad (8)$$

where $b(T)$ is a coefficient calibrated for different spectral ordinated.

The grey area in Figure 10a shows the interval of the separation distances between the buildings belonging to the case-study portfolio; it is possible to observe that the correlation coefficients in this area are high, and therefore the correlation needs to be considered. Finally, the cross-correlation model between spectral accelerations for different vibration periods, proposed by Baker and Cornell (2006) is adopted (Figure 10b), as also suggested by Weatherill et al. (2014), Cimellaro (2013), and as emphasized by studies on the compatibility of American and Italian GMPE models (Scassera et al., 2009):

$$\rho(T_1, T_2) = 1 - cos\left[\frac{\pi}{2} - \left(0.359 + 0.163 \cdot I \cdot ln\frac{T_{Min}}{0.189}\right) \cdot ln\frac{T_{Max}}{T_{Min}}\right] \quad (9)$$

where I is a binary indicator and T_{Min} and T_{Max} are the minimum and the maximum between T_1 and T_2, respectively.

It is worth noting that the coefficients of spatial correlation are available for few values of vibration periods. Therefore, only few spectral accelerations can be simulated within the stochastic simulation approach: PGA, S_a(T=0.2s), S_a(T=0.3s), S_a(T=0.5s), S_a(T=1.0s). This limitation, on one hand reduces the computational demand of the problem (i.e. the dimensions of the covariance matrixes presented in Section 2.1 are significantly reduced); on the other hand, it requires a simplification of the vibration periods of the buildings within the portfolio. Specifically, after a preliminary approximation of the vibration period to the first decimal digit that lead to the clear identification of the classes having period 0.2s and 0.3s, all the structures with period between 0.3s and 0.6s are associated to the class 0.5s, and all the buildings with period larger than 0.6s are associated to the class of structures with 1.0s vibration period.

3.6 The record selection for the 1-D linear and non-linear site response analysis

As anticipated in Section 3.2, both linear and non-linear mono-dimensional site response analyses are carried out for the 6,156 cells covering the entire case study area for which detailed geotechnical properties of the subsoil are available. To perform a site response analysis, a set of ground motions is needed. In this study, natural strong motions recorded on rock, associated to normal faulting (same as the Irpinia earthquake) available in the ITACA database (Luzi et al., 2017) are selected. Specifically, both horizontal components of 150 records (i.e. 300 accelerograms in total) having magnitude between 4 and 7 with epicentral distance between 0 km and 30 km are used. The large number of earthquake records ensure a robust estimate of the *SRF(T)* (Papaspiliou et al., 2012).

Figure 11a shows the distribution of the epicentral distances and magnitude values of the selected seismic events. The limits in terms of magnitude and distance are selected according to the seismic disaggregation of the city of Benevento (Barani et al., 2009). The adopted set of ground motions contains also two records of the Irpinia earthquakes, i.e. the two records in the dashed ellipse in Figure 11a.

Grey lines in Figure 11b show the geometric mean of the response spectra of the two components for each of the 150 records. On the same plot, the continuous black line and the dashed black lines represent the median and the variability of the set, respectively. Finally, the blue and red lines show the geometric mean of the response spectra of the two records of the Irpinia event. It is worth noting that these two events, differently from all the others, present large values of spectral acceleration also for large values of T_1.

4 RESULTS AND DISCUSSION

In this Section, first, the microzonation results obtained from the site response analyses are shown and discussed. Second, the hazard model, i.e., the shakemaps for the Irpina earthquake,

514 are briefly presented. Finally, the influence of the five cases adopted to calculate the *SRF(T)*
515 on the seismic risk at urban scale is analyzed. Moreover, seismic risk maps at urban scale are
516 proposed as a new *Risk-oriented microzonation.*
517
518 **4.1 Microzonation**
519 For each of the 6,156 cells covering the entire case-study area, a Level-3 microzonation study
520 (SMWG, 2015) was conducted; specifically, both linear and non-linear mono-dimensional
521 propagation analyses were performed considering both horizontal components of 150 natural
522 records. Specifically, for each record, the two horizontal components were applied separately
523 in SHAKE91 to the outcropping bedrock, they were deconvoluted at the base of the deformable
524 soil column, and then propagated in the soil column. The response spectra of the propagated
525 records at the top of the soil column (i.e., the deformable soil outcrop) were computed and
526 stored. The *SRF(T)* associated to the i^{th} event was obtained as the ratio between the geometric
527 mean of the two spectra of the two components at the outcropping soil and the geometric mean
528 of the two spectra of the two components of the input. This definition of *SRF(T)* is coherent
529 with the adopted GMPE; in fact, the Bindi et al.' GMPE was fitted using the geometric mean
530 of the two horizontal components of the considered seismic intensity measures. The final
531 *SRF(T)* (that is used in the final representations of this paper and in the risk assessment) was
532 obtained as the average of the 150 site response factors obtained from the 150 records.
533 Figure 12 shows *SRF(T)* maps, obtained by means of non-linear analyses, for PGA
534 (Figure 12a), Sa(T=0.3s) (Figure 12b), Sa(T=0.5s) (Figure 12c), and Sa(T=1.0s) (Figure 12d).
535 Linear analyses return similar results and they are not shown here for the sake of brevity. Such
536 maps show that the maximum amplification is obtained for vibration periods between 0s (e.g.,
537 PGA) and 0.3s. Moreover, de-amplification occurs (*SRF(T)* no smaller than 0.9) on
538 outcropping rock along latitude of approximately 41.125° (see also Figure 4b). Finally, it is

539 worth noting that the spatial distribution of *SRF(T)* reflects (with an inverse relationship) the
540 distribution of the shear wave velocities (Figure 4b).

541 Figure 13 shows the maps of the vibration periods for which the maximum SRF(T) is
542 obtained, both in linear (Figure 13a) and non-linear (Figure 13b) regime. The maximum
543 amplification is obtained for vibration periods varying between 0s and 0.2s. Maximum
544 amplification can be observed for period equal to 0.3s only locally. According to these results
545 and considering the distribution of vibration periods presented in Figure 7c, it emerges that
546 more than half of the considered portfolio of structures can suffer high local amplification
547 effects. The black spots in Figure 13 show the area where de-amplification can occur, and
548 therefore it is not possible to compute a vibration period for which the maximum spectral
549 amplification occurs.

550 Finally, Figure 14 shows the comparison of the *SRF(T)* proposed by Bindi et al.'GMPE
551 (the yellow circles) with the *SRF(T)* calculated from the linear (black dashed line) and non-
552 linear (black continuous) analyses, obtained averaging the *SRF(T)* for all the cells classified as
553 soil B (Figure 14a), soil C (Figure 14b) and soil E (Figure 14c). These presented results are
554 coherent with previous alternative studies for the same case study area (e.g. Santucci de
555 Magistris et al., 2004; 2014; Di Giulio et al., 2008; Improta et al., 2005). For the soil B, the
556 GMPE-based and the analysis-based *SRF(T)* corresponding to the PGA are almost coincident;
557 on the contrary, for periods lower than 0.2s and larger than 0.2s, the GMPE-based *SRF(T)* are
558 smaller and bigger than the analysis-based *SRF(T)*, respectively. For the soil C, the trend is
559 similar to the one explained for the soil B, with the difference that also the *SRF(T)*
560 corresponding to PGA is smaller with respect to the analyses results. Finally, for the soil E,
561 GMPE-based *SRF(T)* are much larger than the analyses-based *SRF(T)* for period lower than
562 0.2s; *SRF(T)* are almost coincident in the range between 0.2s and 0.7s; finally, for period larger
563 than 0.7s, GMPE-based *SRF(T)* are again larger than those obtained via mono-dimensional

propagation. Similar trends in the differences between *SRF(T)* computed in different manner can be observed using any alternative similar GMPE (Luzi et al., 2011; Cauzzi et al., 2015; Bindi et al., 2015). On the same figure, the *SRF(T)* obtained propagating the Irpinia records only are presented (the blue lines). It is possible to observe that the *SRF(T)* shape is like the one obtained considering all the records, and the general comments on the comparison with the GMPE-based *SRF(T)* drawn before are still valid for this case. The differences observed between GMPE-based and analysis-based *SRF(T)* can lead to significant differences on the spectral amplification, and ultimately on the risk assessment. Such differences between GMPE-based and analysis-based *SRF(T)*, that were observed also in other studies (Smerzini et al., 2011; Thompson and Wald, 2016), can be due to a plethora of reasons. For example, GMPE-based amplification factors are obtained by means of statistical analyses of several events, and some authors suggest that GMPE-based amplification factors should be used only if the site-specific V_S profile is consistent with the range of profiles used to derive the functional form of the GMPE. Moreover, the large amplification that is obtained for high values of the vibration period can be a consequence of bi-dimensional of tri-dimensional effects that cannot be caught by the mono-dimensional analysis (Kwok and Stewart, 2006). Finally, the GMPE-based amplification factors have a strong limitation, they are not continuous functions of the V_{S30} but a class-based discrete functions that provide different values of amplification even for soils with very similar values of V_{S30} close to the boundaries of different classes. Only recent GMPE models provide amplification factors as continuous function of V_{S30} (e.g., Boore et al., 2014).

4.2 Irpinia earthquake shakemaps

According to Section 2.1, 10,000 spatially correlated and cross-correlated shakemaps are generated to replicate the 1980 Irpinia event. Figures 15a and 15c show a single-simulation shakemap on rock for PGA and Sa(T=0.2), respectively. It is possible to observe that the spatial

589 correlation is guaranteed; this is even more evident looking at the maps of the residuals of PGA
590 (Figures 15b) and Sa(T=0.2) (Figures 15d) with respect to their corresponding central values.
591 At the same time also the cross-correlation is guaranteed. This is demonstrated by Figure 16.
592 Specifically, Figure 16a shows several intensity measures generated within the same simulation
593 for three grid cells categorized as Soil B, Soil C and Soil E. The distribution of the intensity
594 measures resembles a spectral shape that is expected from the simple application of the GMPE.
595 The same result is obtained averaging the intensity measures over the 10,000 simulations for
596 the same three grid cells (Figure 16b).

597 It is worth noting that the five cases of site response presented in Section 3.2 are built on
598 the basis of the same 10,000 hazard simulations that are performed only once considering
599 *SRF(T)* equal to one. This assumption simplifies the final comparison between the five different
600 hypotheses of site response.

601

602 **4.3 Seismic risk at urban scale: the role of site amplification**

603 In this section the effects induced on the risk assessment by different approaches to the
604 microzonation are investigated. Figure 17 shows the frequency of occurrence of damage states,
605 over the 10,000 simulations, for reinforced concrete (Figure 17a) and masonry structures
606 (Figure 17b) for the five cases of site response analysis. Reinforced concrete structures
607 experience mainly no damage (i.e., DS0), meanwhile, masonry structures experience mainly
608 DS1; for the case of masonry structures, higher damage states are more frequent with respect
609 to reinforced concrete structures. This is a direct result of the more vulnerable nature of
610 masonry structures with respect to reinforced concrete structures.

611 Three main comments about the effect of site response on damage distribution can be
612 done. First, neglecting the site response (i.e., *SRF(T)*=1) leads to an underestimation of the
613 structural damage. This is an expected result; in fact, in general, considering the site response

leads to an amplification of the ground acceleration. Second, for reinforced concrete structures, the Level-2 analyses (i.e., $V_{S30,USGS}$-based and $V_{S30,Test}$-based site analyses) lead to an over-estimation of the damage. Third, for masonry structures, adopting a V_{S30}-based approach, or a more refined Level-3 site response, does not lead to any difference in damage distribution. The reason of the last two comments can be explained looking at the differences between the *SRF(T)* calculated with the rigorous site analyses and those provided by the GMPE in Figure 14. In fact, the vulnerability of masonry structures is determined as function of the PGA; many of the masonry structures in the investigated portfolio are located on soil B. For this soil, the rigorous and simplified *SRF(T)* values are very similar, therefore no differences in the hazard can be observed and consequently no difference in the final damage is expected. On the contrary, the vulnerability of reinforced concrete structures is defined as function of the $Sa(T_1)$. Most reinforced concrete structures are located on soil B and C; for these soils, the *SRF(T)* calculated for period larger than 0.2s, that are the periods of the RC structures in the considered portfolio, are significantly lower than the *SRF(T)* values provided by the GMPE. Therefore, the hazard computed by means of the rigorous Level-3 site response is lower than that calculated by means of a simpler Level-2 analysis, and therefore the expected damage is lower. This thorough description of the damage distribution leads to peculiar characteristics of the overall loss curves.

Figure 18a shows the loss curves corresponding to the five different options of site response analysis. As already observed before, when the site response is neglected (case 1), the damage states are underestimated and therefore the loss curve is the lowest. When the *SRF(T)* is considered (cases 2 to 5), loss curves tend to coincide up to a probability of about 8%; for more rare event (below 8% of probability), Level-2 analyses (cases 2 and 3) lead to an overestimation with respect to Level-3 analyses (case 4 and 5); cases 4 and 5 losses tend to the same estimation that is obtained neglecting the site response. More in general, all the loss

curves tend to the value of the entire portfolio of structures for very rare events (e.g., probability of 10^{-4}).

The observed differences between loss curves can be once again explained de-aggregating losses with respect to the structural typologies. Figure 18b shows the de-aggregation of the loss-curve, obtained with the non-linear mono-dimensional propagation, for masonry and reinforced concrete structures. It is possible to observe that up to 8% probability, the loss is entirely due to the portfolio of masonry structures, that, as explained before, is insensitive to the approach adopted to compute the *SRF(T)*. Once the entire portfolio of masonry structure is lost, the loss curve is governed by only reinforced concrete structures, for which the *SRF(T)* values calculated with more rigorous Level-3 analyses are lower than those obtained by means of Level-2 approaches. Moreover, the loss curves obtained with the more sophisticated analyses tend to coincide with the loss curve obtained neglecting the site response since for these structures the calculated *SRF(T)* is almost equal to one. It is therefore obvious that sophisticated site response analyses can avoid over-conservative estimations for the case of rare events.

Based on the previous results, it is therefore clear that even if site response analyses are particularly time consuming and require many data to be performed, they are essential to have a reliable risk assessment at urban scale, especially in seismic-prone European countries where cities are densely populated and masonry constructions and low-standard RC buildings constitute the vast majority of historical centers (Basaglia et al., 2008).

4.4 Risk-based microzonation

As emphasized in recent studies on risk-targeted seismic hazard, uncertainties in the structural capacity and hazard estimations at different sites lead to an unequal level of risk. This is an undesirable discrepancy; in fact, part of the population will live in buildings with a lower

664 seismic safety than others (Silva et al., 2016). To solve such a discrepancy, two potential
665 approaches are possible: (a) enforce a seismic insurance to inhabitants, or (b) promote risk
666 mitigation strategies by means of disbursement of funds by the national governments. In Italy,
667 for example, latter strategy has been adopted (Cosenza et al., 2018). Obviously, in approaching
668 such a strategy, a govern requires prioritization criteria when several funds requests are raised
669 and there is scarcity of funds. To guaranty a principle of equity between different parts of the
670 population, a potential solution for the prioritization is the definition of risk-based
671 microzonation maps. Such maps can be obtained de-aggregating the loss curves at spatial level
672 identifying potential risk-hotspots in the considered portfolio.

673 Figure 19 shows two maps obtained de-aggregating the loss curve corresponding to the
674 case of non-linear mono-dimensional propagation. Two percentiles are considered, the 50^{th}
675 (Figure 19a) and 16^{th} (Figure 19a) percentiles, representative of the most expected and less
676 frequent loss scenario, respectively. These maps identify the hotspots, that are the areas in the
677 city where there is a high concentration of losses, i.e. high concentration of hazard,
678 vulnerability and risk. Therefore, these maps are the perfect tool to identify the areas on which
679 to prioritize the interventions if new financial resources become available. Such a tool
680 represents the perfect instrument trough which engineers can help stakeholders and policy-
681 makers in the decision process. It is worth noting that such loss maps identify hotspots in the
682 urban area that are not necessarily coincident with the hotspots identified by the classical
683 microzonation presented in Section 4.1. It should be also noted that, in this study, local effects
684 of ground failure are not considered; such effects can drastically change the presented results.
685 Moreover, the risk quantification can be further improved considering a systemic approach
686 where the city can be seen as a complex system of interconnected components (Basaglia et al.,
687 2008; Bozza et al., 2015).
688

5 CONCLUSIONS AND FINAL REMARKS

This study investigated how different procedures for the assessment of the site response affect the seismic risk assessment at urban scale. Specifically, five cases were investigated (i.e., from the neglection of site response up to non-linear mono-dimensional propagation) corresponding to different levels of sophistication of site response analysis (i.e., from Level-1 to Level-3 microzonation). As case study, the main urbanized area in the city of Benevento, Italy, was selected. A scenario-based stochastic framework was adopted for the assessment of the expected loss at urban scale for the 1980 M_w Irpinia earthquake.

Results show that a sophisticated approach to site response, tailored to the properties of the exposed asset, is essential for a reliable assessment of the expected losses as consequence of a seismic event. In fact, it was observed that the risk assessment for masonry structures is not affected by the level of sophistication of the microzonation analysis (i.e. Level-2 or Level-3); differently from masonry structures, the approach to the microzonation can severely affect the risk assessment for concrete structures, especially for rare (i.e., low-probability) events, for which large overestimation of the expected losses were observed if Level-2 methods are adopted. Therefore, as general principle, it is advisable to always perform a preliminary critical analysis of the exposed asset (e.g., identification of the vibration periods) and few rigorous site response analyses for zones of the urban area identified as critical from a Level-2 microzontion.

Finally, a *risk-based microzonation* was proposed. This is an excellent tool for decision making about the redistribution of funds at regional scale for the promotion of risk mitigation guarantying social risk-equality across the urban population.

Several improvements and further advancements can be done. First, this study can be replicated using seismic hazard maps instead of event-based shakemaps, and therefore maps of expected annual loss can be obtained. In this latter case, including information about the seismic hazard, the expected losses could be much lower. Level-3 analyses can be performed

as 2-D or 3-D analyses instead of simple mono-dimensional propagations. Finally, also Structure-Soil-Structure interaction can be considered (Vicencio and Alexander, 2018).

ACKNOWLEDGEMENTS

This work was carried out using the computational facilities of the Advanced Computing Research Center, University of Bristol (http://www.bris.ac.uk/acrc/). The authors also acknowledge Mr. Gianluigi Riccio who has contributed to build the database of buildings.

REFERENCES

AE (2018). Agenzia delle Entrate, Consultazione cartografia catastale – WMS. https://www.agenziaentrate.gov.it/wps/content/nsilib/nsi/schede/fabbricatiterreni/consultazione+cartografia+catastale/servizio+consultazione+cartografia/indice+servizio+consultazione+cartografia. Last access 01/01/2018.

Allen, T.I., & Wald, D.J. (2009). On the use of high-resolution topographic data as a proxy for seismic site conditions (VS 30). Bulletin of the Seismological Society of America, **99**(2A), 935-943.

Ameri, G., Emolo, A., Pacor, F., & Gallovič, F. (2011). Ground-motion simulations for the 1980 M 6.9 Irpinia earthquake (southern Italy) and scenario events. Bulletin of the Seismological Society of America, **101**(3), 1136-1151.

Ansal, A., Akinci, A., Cultrera, G., Erdik, M., Pessina, V., Tönük, G., & Ameri, G. (2009). Loss estimation in Istanbul based on deterministic earthquake scenarios of the Marmara Sea region (Turkey). Soil Dynamics and Earthquake Engineering, **29**(4), 699-709.

Ansal, A., Kurtuluş, A., & Tönük, G. (2010). Seismic microzonation and earthquake damage scenarios for urban areas. Soil Dynamics and Earthquake Engineering, **30**(11), 1319-1328.

Assimaki, D., Ledezma, C., Montalva, G. A., Tassara, A., Mylonakis, G., & Boroschek, R. (2012). Site effects and damage patterns. Earthquake Spectra, **28**(S1), S55-S74.

Atkinson, G. M., & Goda, K. (2013). Probabilistic seismic hazard analysis of civil infrastructure: chapter 1, 3–28, in Handbook of Seismic Risk Analysis and Management of Civil Infrastructure Systems, eds S. Tesfamariam and K. Goda (Cambridge: Woodhead Publishing), 912.

Baker, J.W., & Cornell, C.A. (2006). Correlation of response spectral values for multicomponent ground motions. Bulletin of the seismological Society of America, **96**(1), 215-227.

747 Barani, S., Spallarossa, D., & Bazzurro, P. (2009). Disaggregation of probabilistic ground-
748 motion hazard in Italy. Bulletin of the Seismological Society of America, **99**(5), 2638-2661.
749 Basaglia, A., Aprile, A., Spacone, E., & Pilla, F. (2018). Performance-based seismic risk
750 assessment of urban systems. International Journal of Architectural Heritage, **12**(7-8), 1131-
751 1149.
752 Baturay, M.B., & Stewart, J.P. (2003). Uncertainty and bias in ground-motion estimates from
753 ground response analyses. Bulletin of the Seismological Society of America, **93**(5), 2025-
754 2042.
755 Bazzurro, P., & Cornell, C. A. (2004). Ground-motion amplification in nonlinear soil sites with
756 uncertain properties. Bulletin of the Seismological Society of America, **94**(6), 2090-2109.
757 Bernard, P., & Zollo, A. (1989). The Irpinia (Italy) 1980 earthquake: detailed analysis of a
758 complex normal faulting. Journal of Geophysical Research: Solid Earth, **94**(B2), 1631-1647.
759 Bindi, D., Pacor, F., Luzi, L., Puglia, R., Massa, M., Ameri, G., & Paolucci, R. (2011). Ground
760 motion prediction equations derived from the Italian strong motion database. Bulletin of
761 Earthquake Engineering, **9**(6), 1899-1920.
762 Bindi, D., Massa, M., Luzi, L., Ameri, G., Pacor, F., Puglia, R., & Augliera, P. (2014). Pan-
763 European ground-motion prediction equations for the average horizontal component of
764 PGA, PGV, and 5%-damped PSA at spectral periods up to 3.0 s using the RESORCE
765 dataset. Bulletin of earthquake engineering, **12**(1), 391-430.
766 Boore, D. M., Stewart, J. P., Seyhan, E., & Atkinson, G. M. (2014). NGA-West2 equations for
767 predicting PGA, PGV, and 5% damped PSA for shallow crustal earthquakes. Earthquake
768 Spectra, **30**(3), 1057-1085.
769 Bozza, A., Asprone, D., & Manfredi, G. (2015). Developing an integrated framework to
770 quantify resilience of urban systems against disasters. Natural Hazards, **78**(3), 1729-1748.

771 Brandenberg, S.J., Ballana, N., Shantz, T. (2010). Shear Wave Velocity as a Statistical
772 Function of Standard Penetration Test Resistance and Vertical Effective Stress at Caltrans
773 Bridge Sites. PEER Report 2010/03, Pacific Earthquake Engineering Research Centre,
774 University of California, Berkeley, California, United States of America.
775 Bray, J., Rollins, K., Hutchinson, T., Verdugo, R., Ledezma, C., Mylonakis, G., ... & Kayen,
776 R. (2012). Effects of ground failure on buildings, ports, and industrial facilities. Earthquake
777 Spectra, **28**(S1), S97-S118.
778 Calvi, G. M. (1999). A displacement-based approach for vulnerability evaluation of classes of
779 buildings. Journal of Earthquake Engineering, **3**(03), 411-438.
780 Cauzzi, C., Faccioli, E., Vanini, M., & Bianchini, A. (2015). Updated predictive equations for
781 broadband (0.01–10 s) horizontal response spectra and peak ground motions, based on a
782 global dataset of digital acceleration records. Bulletin of Earthquake Engineering, **13**(6),
783 1587-1612.
784 CDB, Comune Di Benevento website (2018). http://www.comune.benevento.it/bn2_pagine
785 /notizie/puc.php. *In Itlian*. Last access 01/01/2018.
786 Chávez-García, F. J., & Faccioli, E. (2000). Complex site effects and building codes: making
787 the leap. Journal of seismology, **4**(1), 23-40.
788 Chilès, J.-P., Delfiner, P. (2012). Geostatistics: Modeling Spatial Uncertainty, 2nd Edition.
789 John Wiley & Sons., Hoboken, NJ, 699 pp.
790 Ciancimino, A., Foti, S., & Lanzo, G. (2018). Stochastic analysis of seismic ground response
791 for site classification methods verification. Soil Dynamics and Earthquake Engineering,
792 **111**, 169-183.
793 Cimellaro, G. P. (2013). Correlation in spectral accelerations for earthquakes in Europe.
794 Earthquake Engineering & Structural Dynamics, **42**(4), 623-633.

795 Convertito, V., Iervolino, I., & Herrero, A. (2009). Importance of mapping design earthquakes:
796 insights for the Southern Apennines, Italy. Bulletin of the Seismological Society of
797 America, **99**(5), 2979-2991.
798 Cornell, C. A. (1968). Engineering seismic risk analysis. Bulletin of the Seismological Society
799 of America, **58**(5), 1583–1606.
800 Cornell, C.A., & Krawinkler, H. (2000). Progress and challenges in seismic performance
801 assessment, PEER Center News 3, 4 p.
802 Cosenza, E., Del Vecchio, C., Di Ludovico, M., Dolce, M., Moroni, C., Prota, A., & Renzi, E.
803 (2018). The Italian guidelines for seismic risk classification of constructions: technical
804 principles and validation. Bulletin of Earthquake Engineering, 1-31. DOI:
805 https://doi.org/10.1007/s10518-018-0431-8.
806 Crowley, H., & Pinho, R. (2004). Period-height relationship for existing European reinforced
807 concrete buildings. Journal of Earthquake Engineering, **8**(spec01), 93-119.
808 De Risi, R., & Goda, K. (2016). Probabilistic earthquake-tsunami multi-hazard analysis:
809 Application to the Tohoku Region, Japan. Front Built Environ, **2**, 25. DOI:
810 https://doi.org/10.3389/fbuil.2016.00025.
811 De Risi, R., De Luca, F., Kwon, O.S., & Sextos, A. (2018). Scenario-Based Seismic Risk
812 Assessment for Buried Transmission Gas Pipelines at Regional Scale. Journal of Pipeline
813 Systems Engineering and Practice, **9**(4), 04018018.
814 Di Giulio, G., Improta, L., Calderoni, G., & Rovelli, A. (2008). A study of the seismic response
815 of the city of Benevento (Southern Italy) through a combined analysis of seismological and
816 geological data. Engineering Geology, **97**(3-4), 146-170.
817 Dolce, M., Masi, A., Marino, M., & Vona, M. (2003). Earthquake damage scenarios of the
818 building stock of Potenza (Southern Italy) including site effects. Bulletin of Earthquake
819 Engineering, **1**(1), 115-140.

820 Douglas, J. (2003). Earthquake ground motion estimation using strong-motion records: a
821 review of equations for the estimation of peak ground acceleration and response spectral
822 ordinates. Earth-Science Reviews, **61**(1-2), 43-104.
823 Ebrahimian, H., Jalayer, F., Lucchini, A., Mollaioli, F., & Manfredi, G. (2015). Preliminary
824 ranking of alternative scalar and vector intensity measures of ground shaking. Bulletin of
825 Earthquake Engineering, **13**(10), 2805-2840.
826 EN-1998-1 (2003). Eurocode 8: Design of structures for earthquake resistance – Part 1: General
827 rules, seismic actions and rules for buildings. CEN European Committee for
828 Standardization, Bruxelles, Belgium.
829 Esposito, S., & Iervolino, I. (2011). PGA and PGV spatial correlation models based on
830 European multievent datasets. Bulletin of the Seismological Society of America, **101**(5),
831 2532-2541.
832 Esposito, S., & Iervolino, I. (2012). Spatial correlation of spectral acceleration in European
833 data. Bulletin of the Seismological Society of America, **102**(6), 2781-2788.
834 Esposito, E., Porfido, S., Simonelli, A.L., Mastrolorenzo, G., & Iaccarino, G. (2000).
835 Landslides and other surface effects induced by the 1997 Umbria–Marche seismic sequence.
836 Engineering geology, **58**(3-4), 353-376.
837 Falcone, G., Boldini, D., & Amorosi, A. (2018). Site response analysis of an urban area: A
838 multi-dimensional and non-linear approach. Soil Dynamics and Earthquake Engineering,
839 **109**, 33-45.
840 Foti, S., Hollender, F., Garofalo, F., Albarello, D., Asten, M., Bard, P. Y., ... & Forbriger, T.
841 (2018). Guidelines for the good practice of surface wave analysis: a product of the
842 InterPACIFIC project. Bulletin of Earthquake Engineering, **16**(6), 2367-2420.
843 Franke, K. W., Lingwall, B. N., Zimmaro, P., Kayen, R. E., Tommasi, P., Chiabrando, F., &
844 Santo, A. (2018). A Phased Reconnaissance Approach to Documenting Landslides

Following the 2016 Central Italy Earthquakes. Earthquake Spectra. DOI: https://doi.org/10.1193/082117EQS165M.

Freeman, S. A. (2004). Review of the development of the capacity spectrum method. ISET Journal of Earthquake Technology, **41**(1), 1-13.

Gelagoti, F., Kourkoulis, R., Anastasopoulos, I., Tazoh, T., & Gazetas, G. (2010). Seismic wave propagation in a very soft alluvial valley: sensitivity to ground-motion details and soil nonlinearity, and generation of a parasitic vertical component. Bulletin of the Seismological Society of America, **100**(6), 3035-3054.

Gelagoti, F., Kourkoulis, R., Anastasopoulos, I., & Gazetas, G. (2012). Nonlinear dimensional analysis of trapezoidal valleys subjected to vertically propagating SV waves. Bulletin of the Seismological Society of America, **102**(3), 999-1017.

Gavarini, C. (2001). Seismic risk in historical centers. Soil Dynamics and Earthquake Engineering, **21**(5), 459-466.

GN, Geoportale Nazionale (2018). http://www.pcn.minambiente.it/mattm/en/network-services-ogc/. Last access 01/01/2018.

Goda, K., & Hong, H. P. (2008). Spatial correlation of peak ground motions and response spectra. Bulletin of the Seismological Society of America, **98**(1), 354-365.

Goda, K., & Atkinson, G. M. (2009). Probabilistic characterization of spatially correlated response spectra for earthquakes in Japan. Bulletin of the Seismological Society of America, **99**(5), 3003-3020.

Goda, K., & Atkinson, G. M. (2010). Intraevent spatial correlation of ground-motion parameters using SK-net data. Bulletin of the Seismological Society of America, **100**(6), 3055-3067.

Goda, K., & De Risi, R. (2018). Multi-hazard loss estimation for shaking and tsunami using stochastic rupture sources. International journal of disaster risk reduction, **28**, 539-554.

870 Goda, K., & De Risi, R. (2017). Probabilistic Tsunami Loss Estimation Methodology:
871 Stochastic Earthquake Scenario Approach. Earthquake Spectra, **33**(4), 1301-1323.
872 Goda, K., Petrone, C., De Risi, R., & Rossetto, T. (2017). Stochastic coupled simulation of
873 strong motion and tsunami for the 2011 Tohoku, Japan earthquake. Stochastic
874 Environmental Research and Risk Assessment, **31**(9), 2337-2355.
875 Grasso, S., & Maugeri, M. (2009). The seismic microzonation of the city of Catania (Italy) for
876 the maximum expected scenario earthquake of January 11, 1693. Soil Dynamics and
877 Earthquake Engineering, **29**(6), 953-962.
878 Grasso, S., & Maugeri, M. (2014). Seismic microzonation studies for the city of Ragusa (Italy).
879 Soil Dynamics and Earthquake Engineering, **56**, 86-97.
880 GRC, Geoportale Regione Campania (2018). https://sit2.regione.campania.it/content/piano-
881 territoriale-regionale-0. Last access 01/01/2018.
882 Grünthal, G. (1998). European macroseismic scale 1998. European Seismological Commission
883 (ESC). Chaiers du Centre Européen de Géodynamique et de Séismologie, vol. 15
884 Luxembourg.
885 Iannaccone, G., Improta, L., Biella, G., Castellano, M., Deschamps, A., De Franco, R., ... &
886 Zollo, A. (1995). A study of local site effects in Benevento (Southern Italy) by the analysis
887 of seismic records of explosions. Annali di Geofisica, **38**(3-4), 411-427.
888 Idriss, J., & Sun, J.I. (1992). SHAKE91- A computer program for conducting equivalent linear
889 seismic response analyses of horizontally layered soils deposits, University of California,
890 Davis.
891 Iervolino, I., Galasso, C., & Cosenza, E. (2010). REXEL: computer aided record selection for
892 code-based seismic structural analysis. Bulletin of Earthquake Engineering, **8**(2), 339-362.
893 Iervolino, I. (2016). Soil ‐ Invariant Seismic Hazard and Disaggregation. Bulletin of the
894 Seismological Society of America, **106**(4), 1900-1907.

Improta, L., Di Giulio, G., & Rovelli, A. (2005). Variations of local seismic response in Benevento (Southern Italy) using earthquakes and ambient noise recordings. Journal of seismology, **9**(2), 191-210.

ISSMGE, International Society for Soil Mechanics and Geotechnical Engineering (1999). Manual for Zonation on Seismic Geotechnical Hazards (Revised version). Technical Committee for earthquake geotechnical engineering, TC4. The Japanese Geotechnical Society, Tokyo, Japan.

Lancieri, M., & Zollo, A. (2009). Simulated shaking maps for the 1980 Irpinia earthquake, Ms 6.9: Insights on the observed damage distribution. Soil Dynamics and Earthquake Engineering, **29**(8), 1208-1219.

Lanzo, G., Silvestri, F., Costanzo, A., d'Onofrio, A., Martelli, L., Pagliaroli, A., ... & Simonelli, L.A. (2011). Site response studies and seismic microzoning in the Middle Aterno valley (L'Aquila, Central Italy). Bulletin of Earthquake Engineering, **9**(5), 1417.

Luzi, L., Puglia, R., Pacor, F., Gallipoli, M. R., Bindi, D., & Mucciarelli, M. (2011). Proposal for a soil classification based on parameters alternative or complementary to Vs, 30. Bulletin of Earthquake Engineering, **9**(6), 1877-1898.

Luzi, L., Pacor, F., & Puglia, R. (2017). Italian Accelerometric Archive v 2.3. Istituto Nazionale di Geofisica e Vulcanologia, Dipartimento della Protezione Civile Nazionale. DOI: 10.13127/ITACA.2.3.

Kim, B., Hashash, Y. M., Stewart, J. P., Rathje, E. M., Harmon, J. A., Musgrove, M. I., ... & Silva, W. J. (2016). Relative differences between nonlinear and equivalent-linear 1-D site response analyses. Earthquake Spectra, **32**(3), 1845-1865.

Kwok, A. O., & Stewart, J. P. (2006). Evaluation of the effectiveness of theoretical 1D amplification factors for earthquake ground-motion prediction. Bulletin of the Seismological Society of America, **96**(4A), 1422-1436.

Kotha, S.R., Bazzurro, P., & Pagani, M. (2018). Effects of Epistemic Uncertainty in Seismic Hazard Estimates on Building Portfolio Losses. Earthquake Spectra, **34**(1), 217-236.

Kottke, A. R., & Rathje, E. M. (2013). Comparison of time series and random‐vibration theory site‐response methods. Bulletin of the Seismological Society of America, **103**(3), 2111-2127.

Makra, K., Chávez-García, F. J., Raptakis, D., & Pitilakis, K. (2005). Parametric analysis of the seismic response of a 2D sedimentary valley: implications for code implementations of complex site effects. Soil dynamics and earthquake engineering, **25**(4), 303-315.

Martino, S., Prestininzi, A., & Romeo, R. W. (2014). Earthquake-induced ground failures in Italy from a reviewed database. Natural Hazards and Earth System Sciences, **14**(4), 799.

Maugeri, M., Simonelli, A.L., Ferraro, A., Grasso, S., & Penna, A. (2011). Recorded ground motion and site effects evaluation for the April 6, 2009 L'Aquila earthquake. Bulletin of Earthquake Engineering, **9**(1), 157-179.

McGuire, R.K. (2004). Seismic hazard and risk analysis. Earthquake Engineering Research Institute. P.240.

Miano, A., Jalayer, F., De Risi, R., Prota, A., & Manfredi, G. (2016). Model updating and seismic loss assessment for a portfolio of bridges. Bulletin of Earthquake Engineering, **14**(3), 699-719.

Nakamura, Y. (1989). A Method for Dynamic Characteristics Estimation of Subsurface Using Microtremor on the Ground Surface. Quarterly Report of RTRI, vol. 30, No. 1, Page No. 25 to 33.

Ohta, Y., & Goto, N. (1978). Empirical shear wave velocity equations in terms of characteristic soil indexes. Earthquake engineering & structural dynamics, **6**(2), 167-187.

Oliver, D. S. (2003). Gaussian cosimulation: modelling of the cross-covariance. Mathematical Geology, **35**(6), 681-698.

945 OMI (2018). Osservatorio del Mercato Immobiliare, Agenzia delle Entrate del Govento
946 Italiano. https://wwwt.agenziaentrate.gov.it/geopoi_omi/index.php. Last access
947 01/01/2018.
948 OSM (2018). OpenStreetMap. https://www.openstreetmap.org. Last access 01/01/2018.
949 Panzera, F., Rigano, R., Lombardo, G., Cara, F., Di Giulio, G., & Rovelli, A. (2011). The role
950 of alternating outcrops of sediments and basaltic lavas on seismic urban scenario: the study
951 case of Catania, Italy. Bulletin of Earthquake Engineering, **9**(2), 411-439.
952 Papaspiliou, M., Kontoe, S., & Bommer, J. J. (2012). An exploration of incorporating site
953 response into PSHA—Part I: Issues related to site response analysis methods. Soil
954 Dynamics and Earthquake Engineering, **42**, 302-315.
955 Psarropoulos, P. N., Tazoh, T., Gazetas, G., & Apostolou, M. (2007). Linear and nonlinear
956 valley amplification effects on seismic ground motion. Soils and Foundations, **47**(5), 857-
957 871.
958 Penna, A. (2005). Applicazione della geostatistica allo studio della risposta sismica locale: la
959 microzonazione sismica della città di Benevento. PhD Thesis in Seismic Risk, University
960 of Naples Federico II (in Italian).
961 Pergalani, F., De Franco, R., Compagnoni, M., & Caielli, G. (2006). Evaluation of site effects
962 using numerical and experimental analyses in Città di Castello (Italy). Soil Dynamics and
963 Earthquake Engineering, **26**(10), 941-951.
964 Pergalani, F., Compagnoni, M., & Petrini, V. (2008). Evaluation of site effects using numerical
965 analyses in Celano (Italy) finalized to seismic risk assessment. Soil Dynamics and
966 Earthquake Engineering, **28**(12), 964-977.
967 Porter, K., Kennedy, R., & Bachman, R. (2007). Creating fragility functions for performance-
968 based earthquake engineering. Earthquake Spectra, **23**(2), 471-489.

969 Ramberg, W., & Osgood, W. R. (1943). Description of stress-strain curves by three parameters.
970 Technical Note No. 902, National Advisory committee for Aeronautics, Wessington, DC.
971 Riga, E., Makra, K., & Pitilakis, K. (2016). Aggravation factors for seismic response of
972 sedimentary basins: A code-oriented parametric study. Soil Dynamics and Earthquake
973 Engineering, **91**, 116-132.
974 Romeo, R. W., & Bisiccia, C. (2006). Risk-oriented seismic microzoning study of an urban
975 settlement. Soil Dynamics and Earthquake Engineering, **26**(10), 899-908.
976 Rossetto, T., & Elnashai, A. (2003). Derivation of vulnerability functions for European-type
977 RC structures based on observational data. Engineering structures, **25**(10), 1241-1263.
978 Rota, M., Penna, A., & Strobbia, C. L. (2008). Processing Italian damage data to derive
979 typological fragility curves. Soil Dynamics and Earthquake Engineering, **28**(10-11), 933-
980 947.
981 Rota, M., Penna, A., & Magenes, G. (2010). A methodology for deriving analytical fragility
982 curves for masonry buildings based on stochastic nonlinear analyses. Engineering
983 Structures, **32**(5), 1312-1323.
984 Rovida, A., Locati, M., Camassi, R., Lolli, B., Gasperini, P. (eds), (2016). CPTI15, the 2015
985 version of the Parametric Catalogue of Italian Earthquakes. Istituto Nazionale di Geofisica
986 e Vulcanologia. doi:http://doi.org/10.6092/INGV.IT-CPTI15
987 Sahin, A., Sisman, R., Askan, A., & Hori, M. (2016). Development of integrated earthquake
988 simulation system for Istanbul. Earth, Planets and Space, **68**(1), 115.
989 Santucci de Magistris, F., d'Onofrio, A., & Sica, S. (2004). A step into the definition of the
990 seismic risk for the city of Benevento (Italy). In: Proceedings of the fifth international
991 conference on case histories in geotechnical engineering, New York City, NY

992 Santucci De Magistris, F., d'Onofrio, A., Penna, A., Puglia, R., & Silvestri, F. (2014). Lessons
993 learned from two case histories of seismic microzonation in Italy. Natural hazards, **74**(3),
994 2005-2035.
995 Scasserra, G., Stewart, J. P., Bazzurro, P., Lanzo, G., & Mollaioli, F. (2009). A comparison of
996 NGA ground-motion prediction equations to Italian data. Bulletin of the Seismological
997 Society of America, **99**(5), 2961-2978.
998 Semblat, J. F. (2010). Modeling seismic wave propagation and amplification in 1D/2D/3D
999 linear and nonlinear unbounded media. International Journal of Geomechanics, **11**(6), 440-
1000 448.
1001 Sextos, A., De Risi, R., Pagliaroli, A., Foti, S., Passeri, F., Ausilio, E., ... & Dashti, S. (2018).
1002 Local site effects and incremental damage of buildings during the 2016 Central Italy
1003 earthquake sequence. Earthquake Spectra. DOI: https://doi.org/10.1193/100317EQS194M.
1004 Silva, V., Crowley, H., & Bazzurro, P. (2016). Exploring risk-targeted hazard maps for Europe.
1005 Earthquake Spectra, **32**(2), 1165-1186.
1006 Smerzini, C., Paolucci, R., & Stupazzini, M. (2011). Comparison of 3D, 2D and 1D numerical
1007 approaches to predict long period earthquake ground motion in the Gubbio plain, Central
1008 Italy. Bulletin of Earthquake Engineering, **9**(6), 2007-2029.
1009 Smerzini, C., Pitilakis, K., & Hashemi, K. (2017). Evaluation of earthquake ground motion and
1010 site effects in the Thessaloniki urban area by 3D finite-fault numerical simulations. Bulletin
1011 of earthquake engineering, **15**(3), 787-812.
1012 Smerzini, C., & Pitilakis, K. (2018). Seismic risk assessment at urban scale from 3D physics-
1013 based numerical modeling: the case of Thessaloniki. Bulletin of Earthquake Engineering,
1014 **16**(7), 2609-2631.
1015 SMWG, Seismic Microzonation Working Group. (2015). Guidelines for Seismic
1016 Microzonation, Conference of Regions and Autonomous Provinces of Italy – Civil

1017 Protection Department, Rome, 2015. http://www.protezionecivile.gov.it/httpdocs
1018 /cms/attach_extra/GuidelinesForSeismicMicrozonation.pdf. Last access 01/01/2018.
1019 Sousa, L., Silva, V., & Bazzurro, P. (2017). Using Open-Access Data in the Development of
1020 Exposure Data Sets of Industrial Buildings for Earthquake Risk Modeling. Earthquake
1021 Spectra, **33**(1), 63-84.
1022 Sousa, L., Silva, V., Marques, M., & Crowley, H. (2018). On the treatment of uncertainty in
1023 seismic vulnerability and portfolio risk assessment. Earthquake Engineering & Structural
1024 Dynamics, **47**(1), 87-104.
1025 Stanko, D., Gülerce, Z., Markušić, S., & Šalić, R. (2019). Evaluation of the site amplification
1026 factors estimated by equivalent linear site response analysis using time series and random
1027 vibration theory based approaches. Soil Dynamics and Earthquake Engineering, **117**, 16-29.
1028 Stewart, J. P., Liu, A. H., & Choi, Y. (2003). Amplification factors for spectral acceleration in
1029 tectonically active regions. Bulletin of the Seismological Society of America, **93**(1), 332-
1030 352.
1031 Stewart, J.P., Klimis, N., Savvaidis, A., Theodoulidis, N., Zargli, E., Athanasopoulos, G., ... &
1032 Margaris, B. (2014). Compilation of a local VS profile database and its application for
1033 inference of VS 30 from geologic‐and terrain‐based proxies. Bulletin of the
1034 Seismological Society of America, **104**(6), 2827-2841.
1035 Thompson, E. M., & Wald, D. J. (2016). Uncertainty in VS 30‐based site response. Bulletin
1036 of the Seismological Society of America, **106**(2), 453-463.
1037 USGS, United States Geological Survey (2017). Global Vs30 Map Server.
1038 https://www.sciencebase.gov/catalog/item/5890c658e4b072a7ac0caef3. Last access
1039 01/01/2018.

1040 Vardanega, P. J., & Bolton, M. D. (2013). Stiffness of clays and silts: Normalizing shear
1041 modulus and shear strain. Journal of Geotechnical and Geoenvironmental Engineering,
1042 **139**(9), 1575-1589.
1043 Vicencio, F., & Alexander, N. A. (2018). Dynamic interaction between adjacent buildings
1044 through nonlinear soil during earthquakes. Soil Dynamics and Earthquake Engineering, **108**,
1045 130-141.
1046 Wair, B.R., DeJong, J.T., Shantz, T. (2012). Guidelines for Estimation of Shear Wave Velocity
1047 Profiles. PEER Report 2012/08, Pacific Earthquake Engineering Research Centre,
1048 University of California, Berkeley, California, United States of America.
1049 Wald, D.J., Worden, B.C., Quitoriano, V., & Pankow, K. L. (2006). ShakeMap manual:
1050 Technical manual, user's guide, and software guide, 156. Reston, VA: United States
1051 Geological Survey.
1052 Wald, D. J., & Allen, T. I. (2007). Topographic slope as a proxy for seismic site conditions and
1053 amplification. Bulletin of the Seismological Society of America, **97**(5), 1379-1395.
1054 Weatherill, G., Esposito, S., Iervolino, I., Franchin, P., & Cavalieri, F. (2014). Framework for
1055 seismic hazard analysis of spatially distributed systems. In SYNER-G: Systemic Seismic
1056 Vulnerability and Risk Assessment of Complex Urban, Utility, Lifeline Systems and
1057 Critical Facilities (pp. 57-88). Springer, Dordrecht.
1058 Weatherill, G. A., Silva, V., Crowley, H., & Bazzurro, P. (2015). Exploring the impact of
1059 spatial correlations and uncertainties for portfolio analysis in probabilistic seismic loss
1060 estimation. Bulletin of Earthquake Engineering, **13**(4), 957-981.
1061

Figure captions

Fig. 1. Risk assessment framework, (a) Area and portfolio of buildings of interest, and seismic sources. (b) Shakemap: simulated seismic scenario, i.e., intensity measures spatially correlated. (c) Intensity measures for each building. (d) Fragility curves. (e) Damage ratios. (f) Loss curve.

Fig. 2 The case study. (a) City location and catalogue of historical earthquakes. (b) Topography of the case study area. (c) Geological map (1:250,000); A1: Recent alluvia, Holocene; A2: Terraced alluvia (late Pleistocene); P: Sandstones and conglomerates (middle Pliocene); C: Fluvio-lacustric deposits (middle Pleistocene); M: Shales, sandstones and marly-limestone (Miocene). (d) Geo-lithological map (1:500,000); AM: Alluvial and mixed soils; SC: Sandstones and conglomerates; Cl: Clays.

Fig. 3 (a) Shear wave velocity and depth (contour) of the bedrock. (b) Geologic Section 1; (c) Geologic Section 2; (d) Geologic Section 3.

Fig. 4 (a) Shear wave velocity and (c) soil classification maps obtained from the USGS global database. (b) Shear wave velocity and (d) soil classification maps based on boreholes data. The black dots represent the locations of the available boreholes.

Fig. 5 Nonlinear soil behavior in terms of (a) shear stiffness reduction and (b) damping increase with the shear deformation.

Fig. 6 (a) GIS database of the considered portfolio of buildings (B1, C1, D1, B2, and C2 represent different area of the city with different real estate values); (b) Distribution of masonry (M) and reinforced concrete (RC) buildings; (c) Distribution of the buildings uses (C: Commercial, P: Productive, R: Residential, T: Tertiary); (d) Distribution of the buildings number of storeys; (e) Distribution of the buildings heights.

1087 **Fig. 7** (a) Adopted empirical relationship between building height and vibration period.
1088 (b) Comparison between the used and an alternative empirical relationship for the
1089 assessment of the vibration period. Distribution of the vibration period for masonry
1090 and reinforced concrete structures.
1091 **Fig. 8** (a) Fragility curves for masonry structures. (b) Fragility curves for reinforced
1092 concrete structures.
1093 **Fig. 9** (a) Activated faults, faulting style and accelerometric station on soil B. (b) Bindi et
1094 al. (2011) GMPE and recorded values of PGA values at the stations shown in (a).
1095 **Fig. 10** (a) Coefficient of spatial correlation for few spectral acceleration values bespoke
1096 for the adopted GMPE. (b) Coefficient of correlation between spectral
1097 accelerations for two different vibration periods (i.e., T1 and T2) recorded at the
1098 same site.
1099 **Fig. 11** (a) Distribution of epicentral distances and magnitude values of the selected events.
1100 (b) Geometric mean of the response spectra of the selected records.
1101 **Fig. 12** Maps of the site response factor for (a) PGA, (b) Sa(T=0.3s), (c) Sa(T=0.5s) and
1102 (d) Sa(T=1.0s) obtained from the non-linear site response analysis.
1103 **Fig. 13** Maps of the vibration period for which the maximum site amplification is obtained
1104 for both (a) linear and (b) non-linear response analyses. Black areas correspond to
1105 de-amplification.
1106 **Fig. 14** GMPE SRF(T) and linear and non-linear average SRF(T) for (a) Soil B, (b) Soil C,
1107 and (c) Soil E.
1108 **Fig. 15** Single realizations of shakemaps and corresponding residual maps for (a,b) PGA
1109 and (c,d) Sa(T=0.2s).
1110 **Fig. 16** Single realizations of shakemaps and corresponding residual maps for (a,b) PGA
1111 and (c,d) Sa(T=0.2s).

Fig. 17 Frequency of damage states observed over the 10,000 simulations for the five cases of site response analysis for (a) reinforced concrete buildings and (b) masonry buildings.

Fig. 18 (a) Loss curves for the five cases of site response analysis. (b) De-aggregation of the losses computed considering the non-linear mono-dimensional propagation for masonry (M) and reinforced concrete (RC) structures.

Fig. 19 Risk maps obtained considering the non-linear mono-dimensional propagation, corresponding to the (a) 50th percentile and to the (b) 16th percentile of the loss curve.

Figures

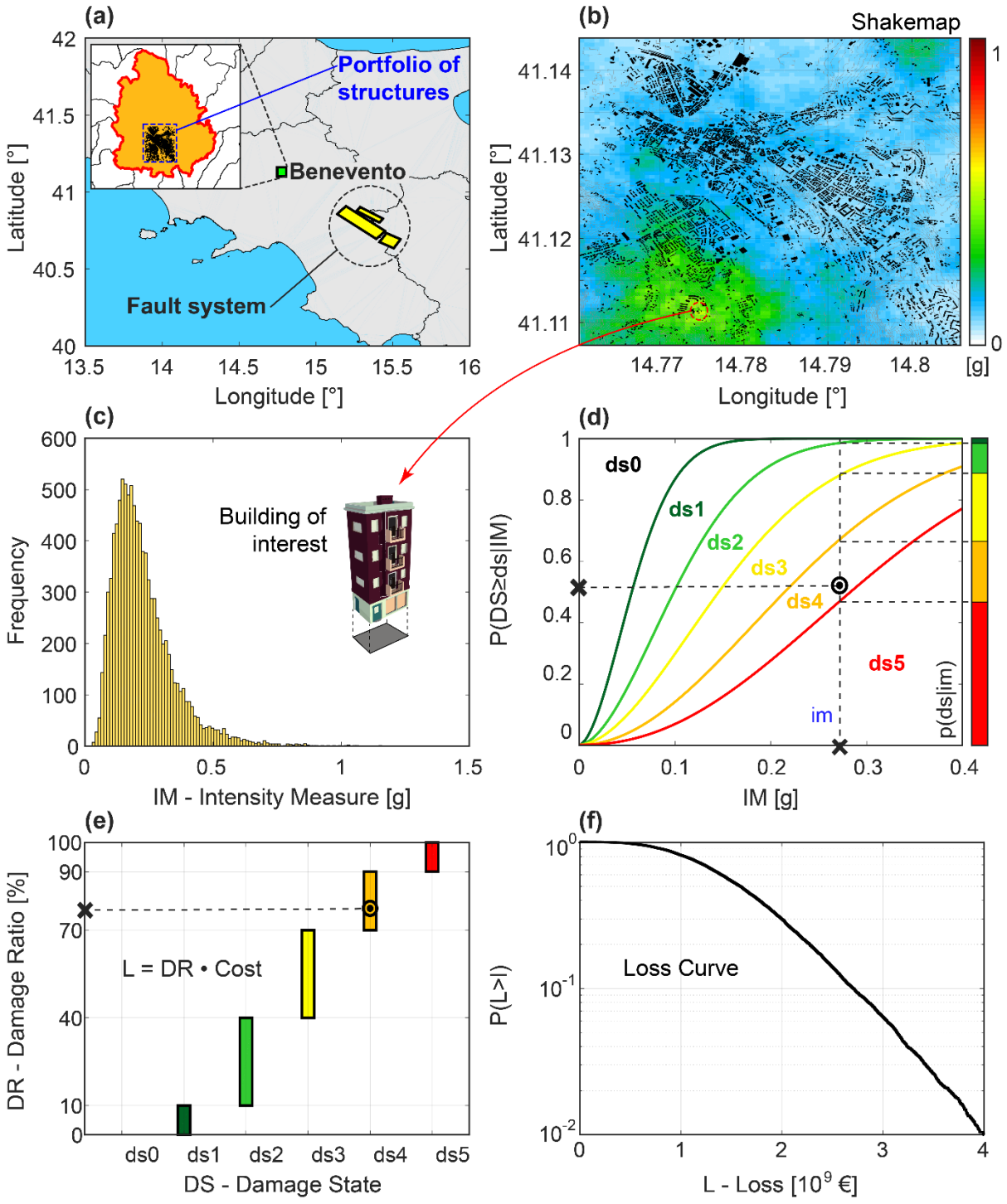

Fig. 1 Risk assessment framework, (a) Area and portfolio of buildings of interest, and seismic sources. (b) Shakemap: simulated seismic scenario, i.e., intensity measures spatially correlated. (c) Intensity measures for each building. (d) Fragility curves. (e) Damage ratios. (f) Loss curve.

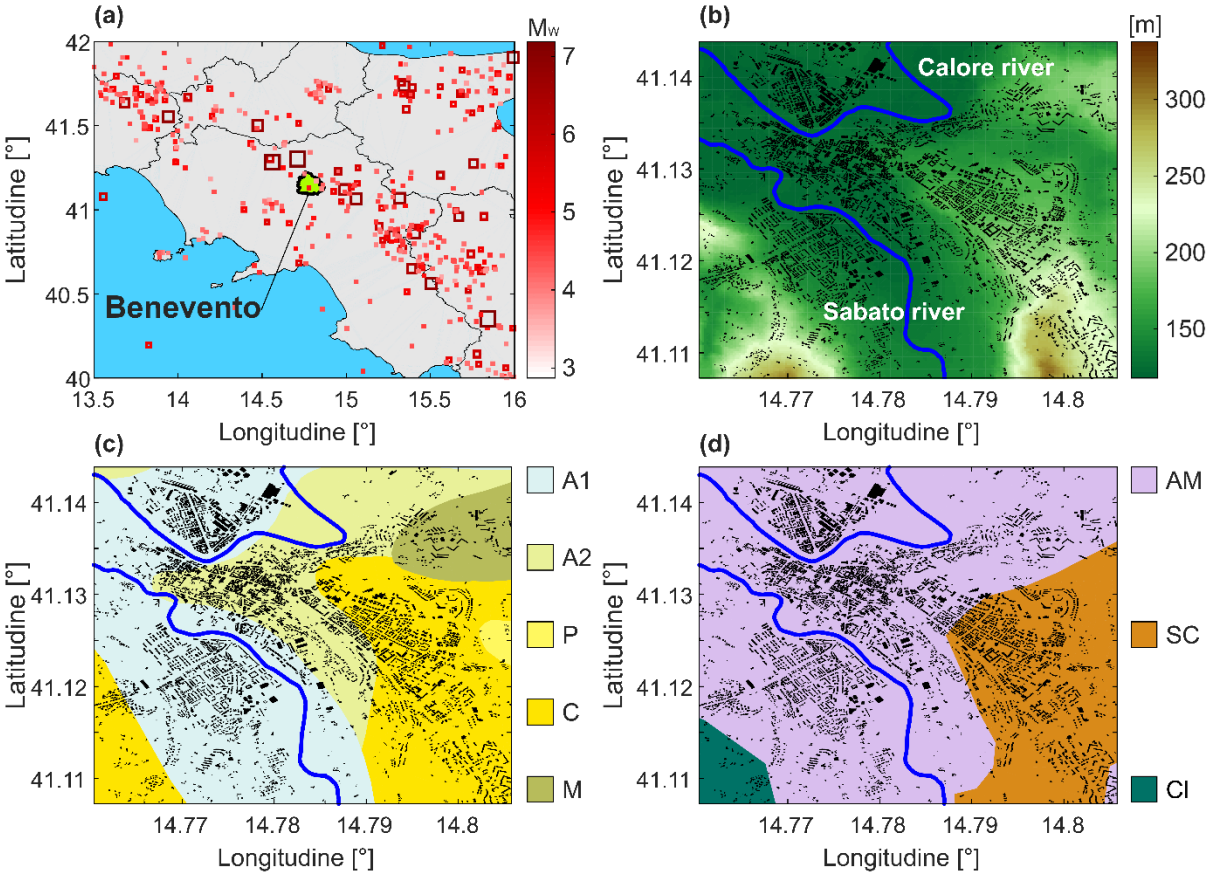

Fig. 2 The case study. (a) City location and catalogue of historical earthquakes. (b) Topography of the case study area. (c) Geological map (1:250,000); A1: Recent alluvia, Holocene; A2: Terraced alluvia (late Pleistocene); P: Sandstones and conglomerates (middle Pliocene); C: Fluvio-lacustric deposits (middle Pleistocene); M: Shales, sandstones and marly-limestone (Miocene). (d) Geo-lithological map (1:500,000); AM: Alluvial and mixed soils; SC: Sandstones and conglomerates; Cl: Clays.

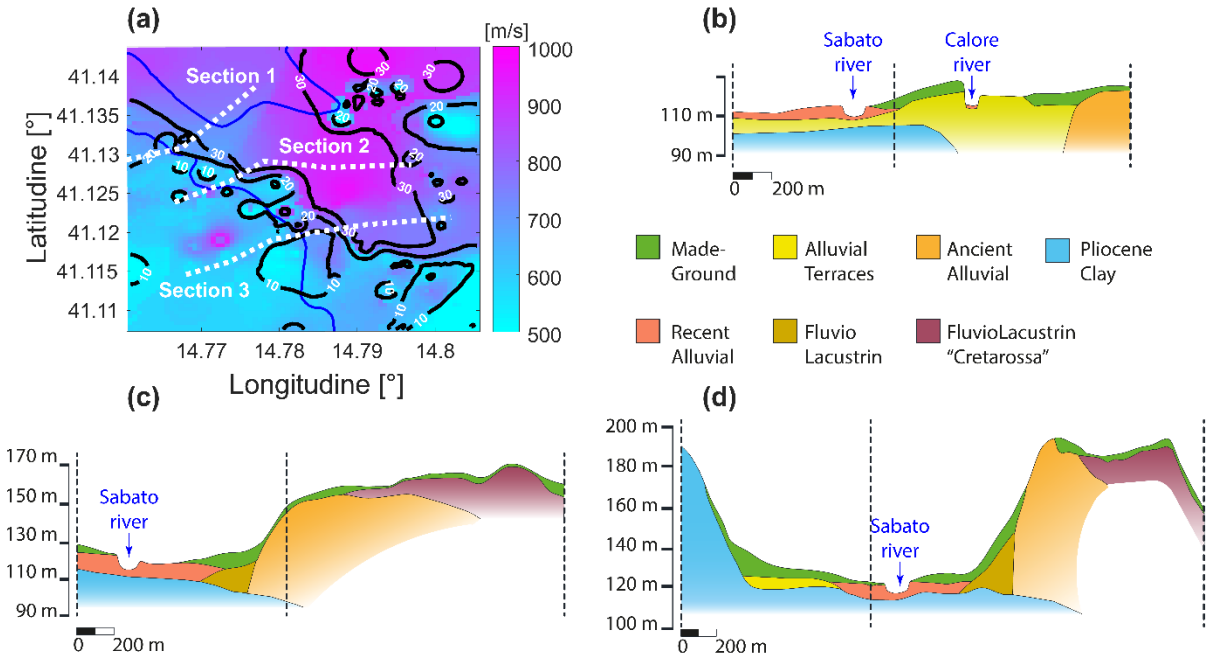

1134

1135 **Fig. 3** (a) Shear wave velocity and depth (contour) of the bedrock. (b) Geologic Section 1; (c)

1136 Geologic Section 2; (d) Geologic Section 3.

1137

1138

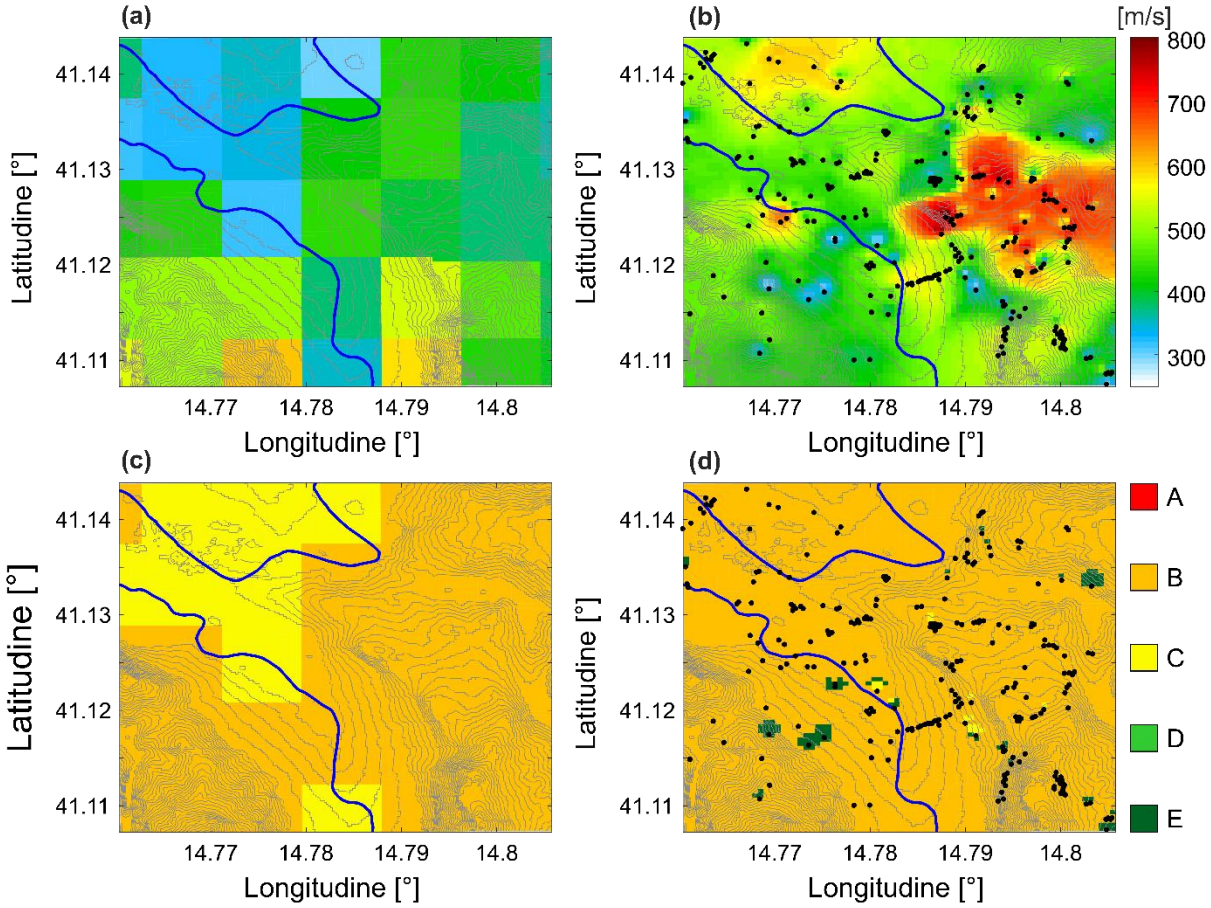

Fig. 4 (a) V_{S30} and (c) soil classification maps obtained from the USGS global database. (b) V_{S30} and (d) soil classification maps based on boreholes data. The black dots represent the locations of the available boreholes.

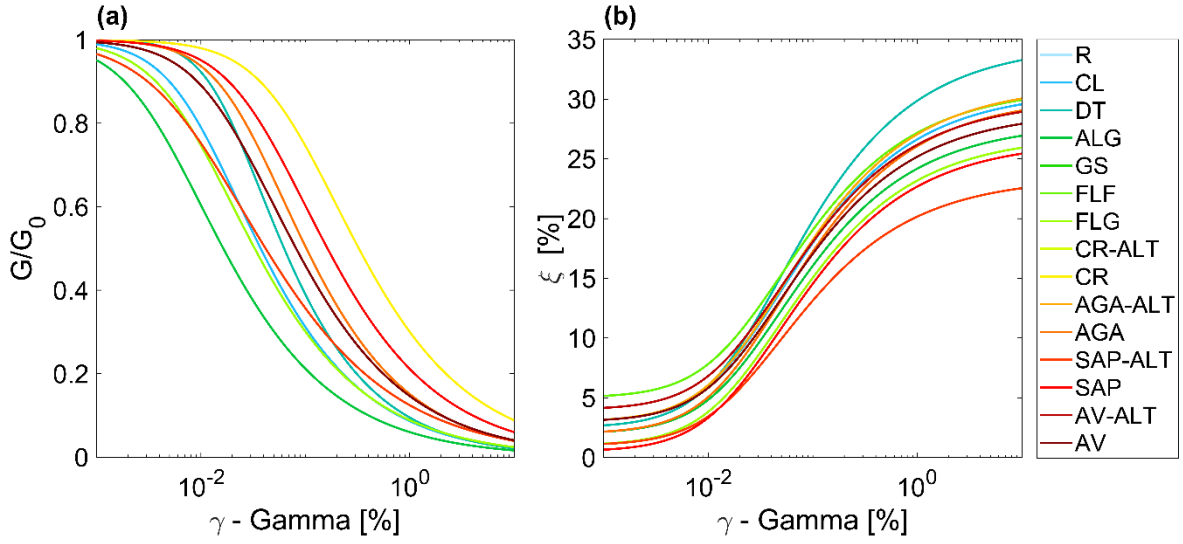

Fig. 5 Nonlinear soil behavior in terms of (a) shear stiffness reduction and (b) damping increase with the shear deformation.

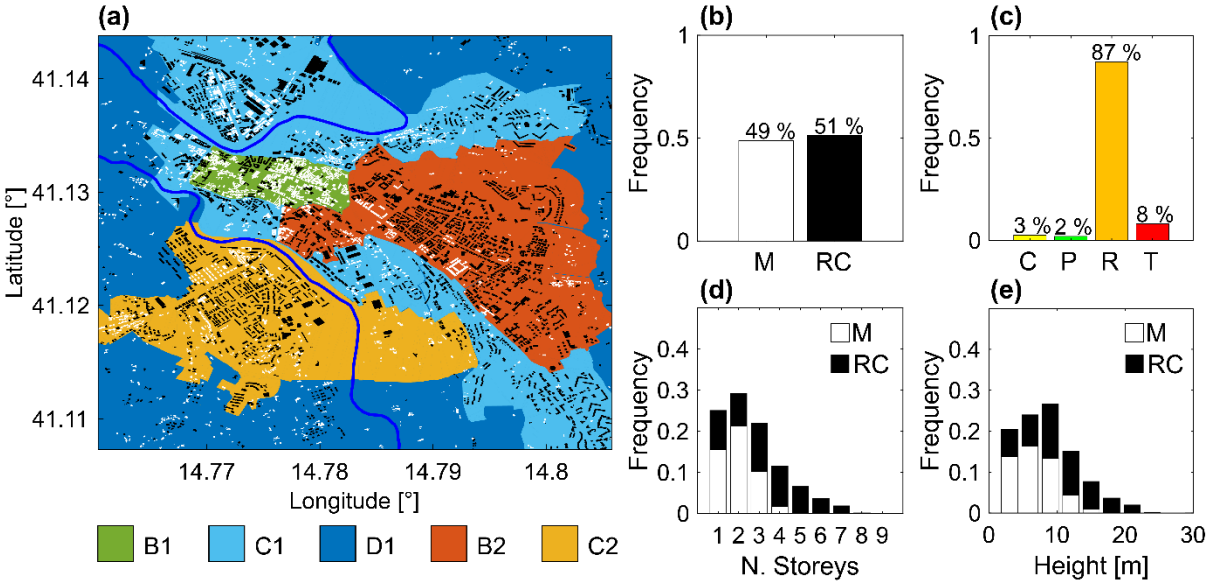

1146

1147 **Fig. 6** (a) GIS database of the considered portfolio of buildings (B1, C1, D1, B2, and C2
1148 represent different area of the city with different real estate values); (b) Distribution of masonry
1149 (M) and reinforced concrete (RC) buildings; (c) Distribution of the buildings uses (C:
1150 Commercial, P: Productive, R: Residential, T: Tertiary); (d) Distribution of the buildings
1151 number of storeys; (e) Distribution of the buildings heights.

1152

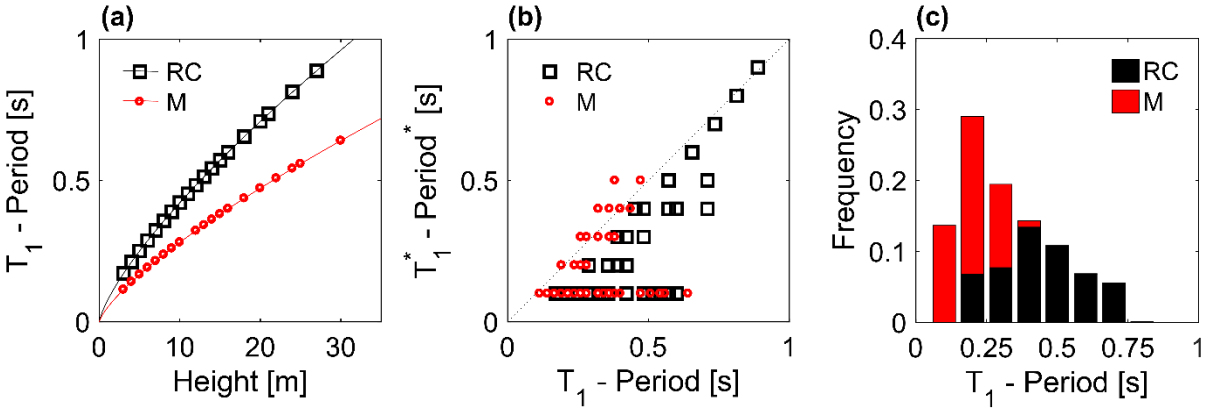

1153

1154 **Fig. 7** (a) Adopted empirical relationship between building height and vibration period. (b)
1155 Comparison between the used and an alternative empirical relationship for the assessment of
1156 the vibration period. Distribution of the vibration period for masonry and reinforced concrete
1157 structures.

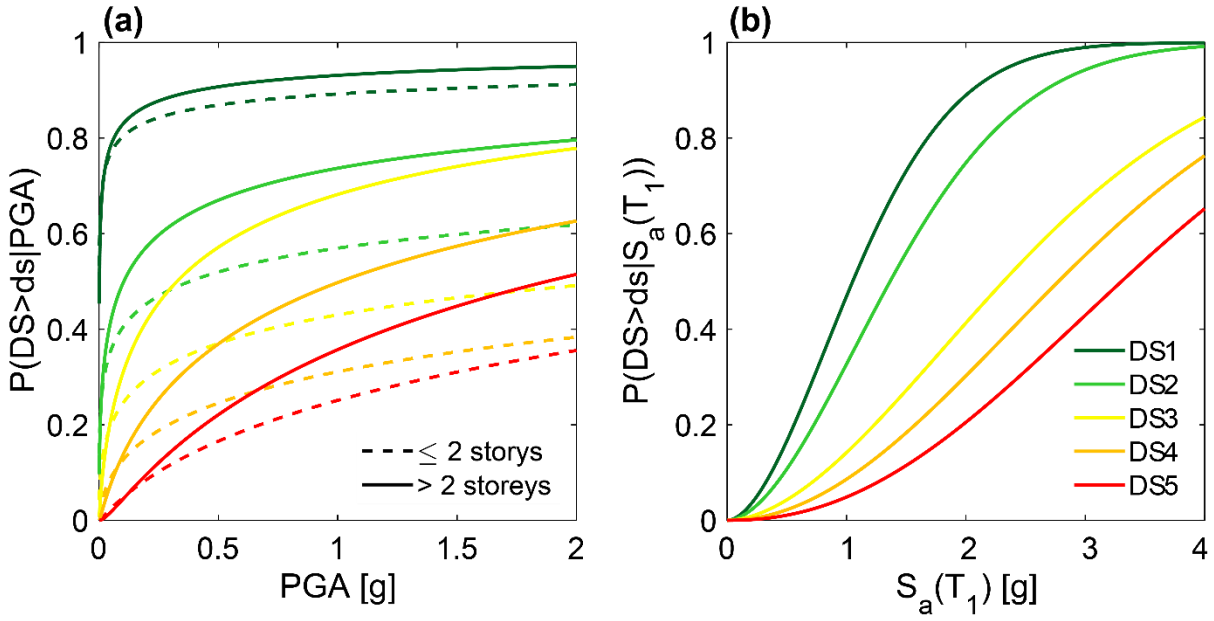

Fig. 8 (a) Fragility curves for masonry structures. (b) Fragility curves for reinforced concrete structures.

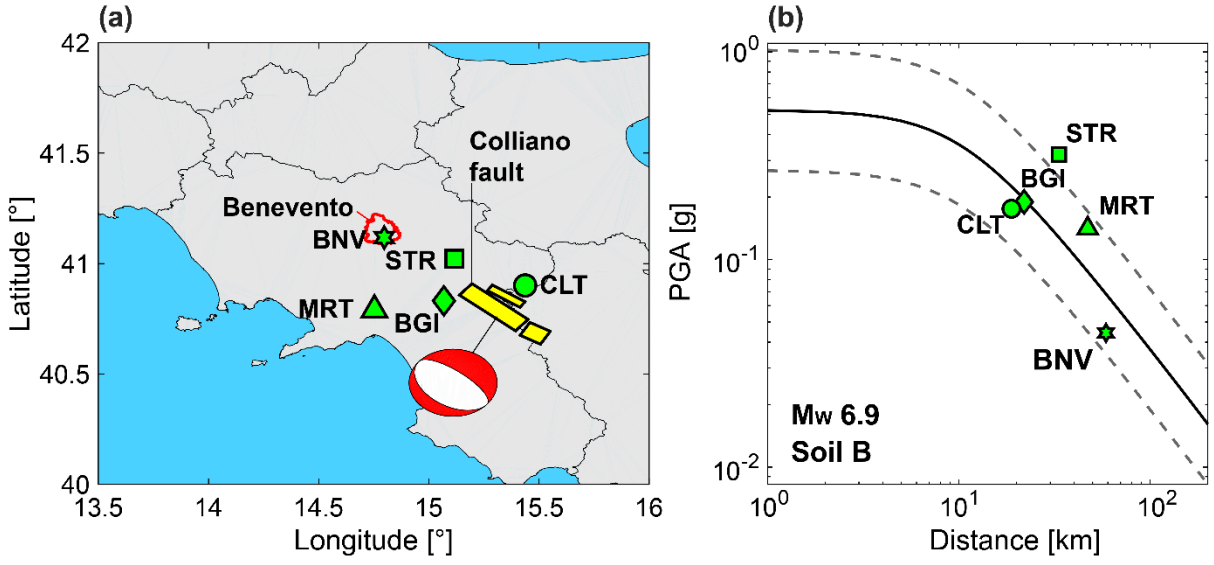

Fig. 9 (a) Activated faults, faulting style and accelerometric station on soil B. (b) Bindi et al. (2011) GMPE and recorded values of PGA values at the stations shown in (a).

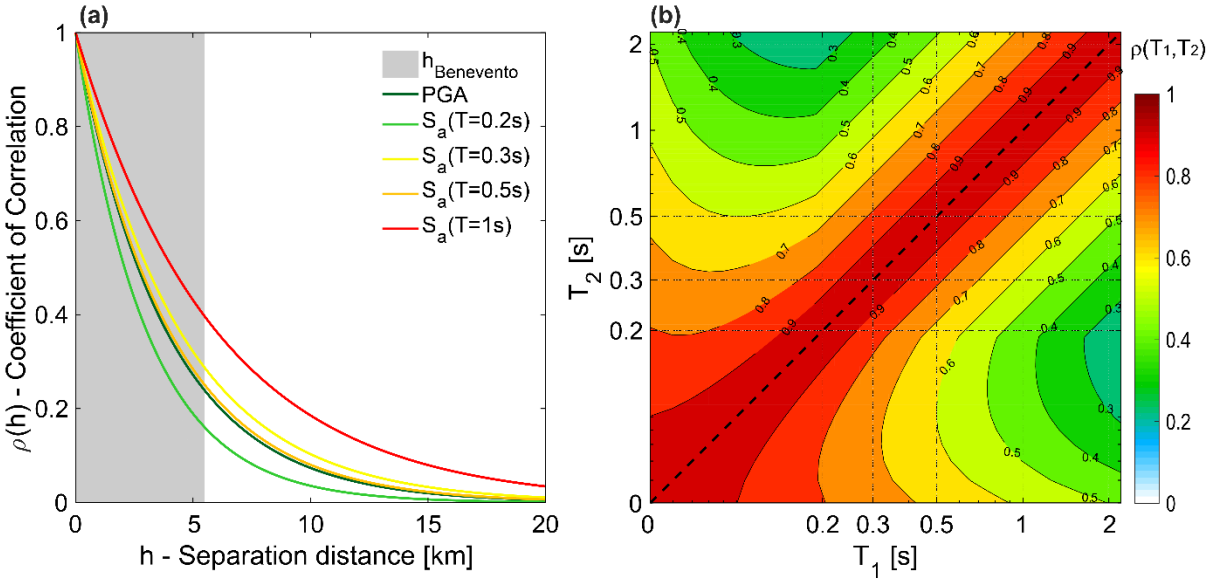

1165

1166 **Fig. 10** (a) Coefficient of spatial correlation for few spectral acceleration values bespoke for

1167 the adopted GMPE. (b) Coefficient of correlation between spectral accelerations for two

1168 different vibration periods (i.e., T_1 and T_2) recorded at the same site.

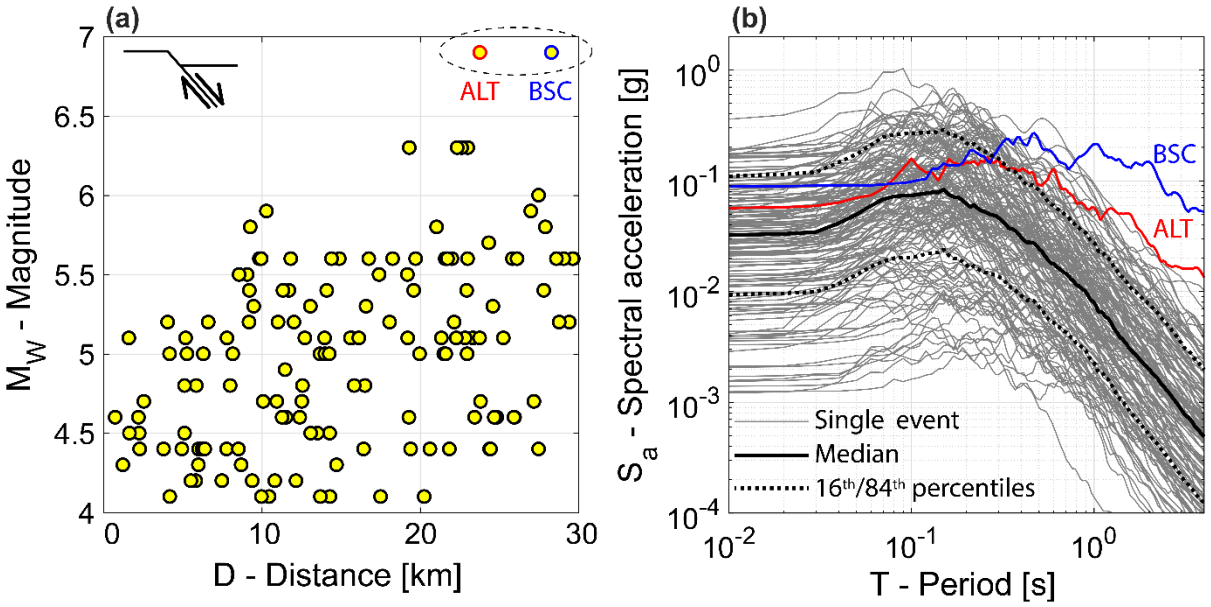

1169

1170 **Fig. 11** (a) Distribution of epicentral distances and magnitude values of the selected events.

1171 (b) Geometric mean of the response spectra of the selected records.

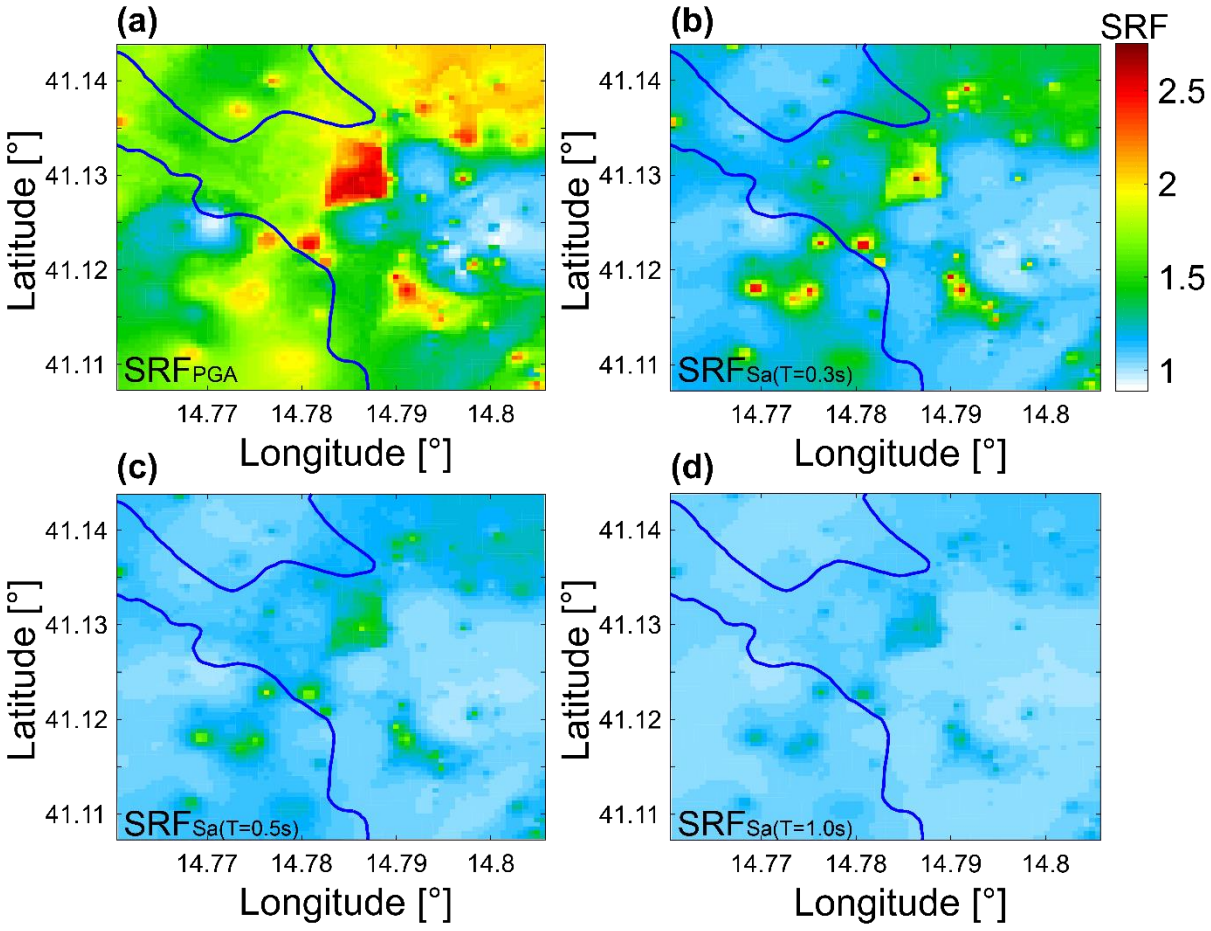

Fig. 12 Maps of the site response factor for (a) PGA, (b) Sa(T=0.3s), (c) Sa(T=0.5s) and (d) Sa(T=1.0s) obtained from the non-linear site response analysis.

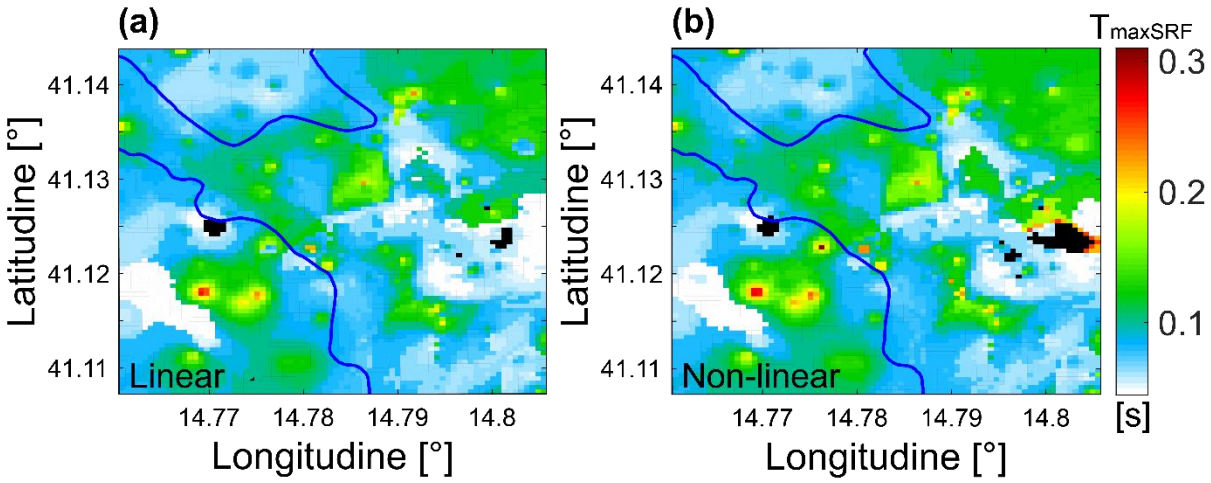

Fig. 13 Maps of the vibration period for which the maximum site amplification is obtained for both (a) linear and (b) non-linear response analyses. Black areas correspond to de-amplification.

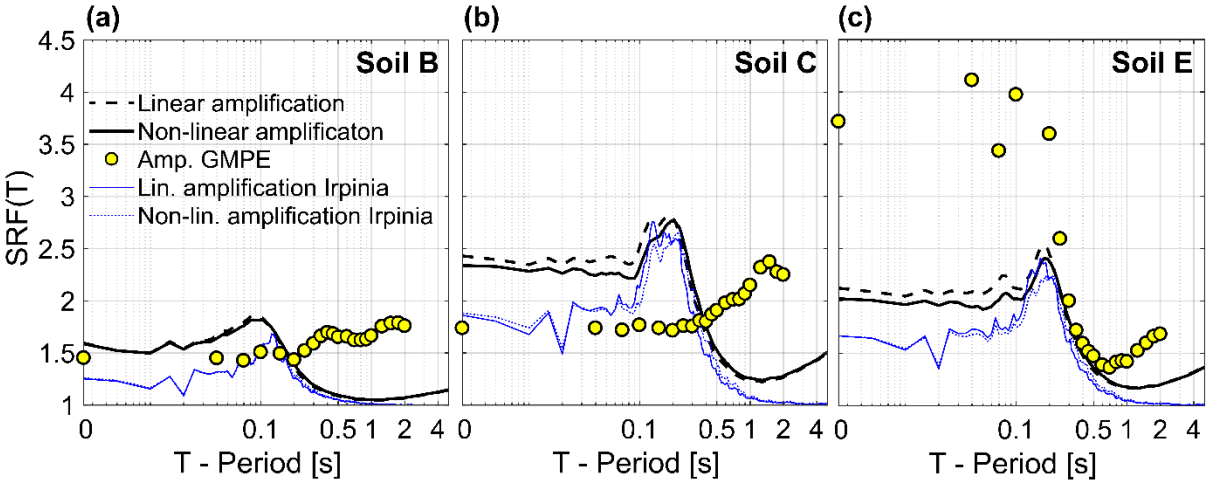

1179

1180 **Fig. 14** GMPE SRF(T) and linear and non-linear average SRF(T) for (a) Soil B, (b) Soil C, and

1181 (c) Soil E.

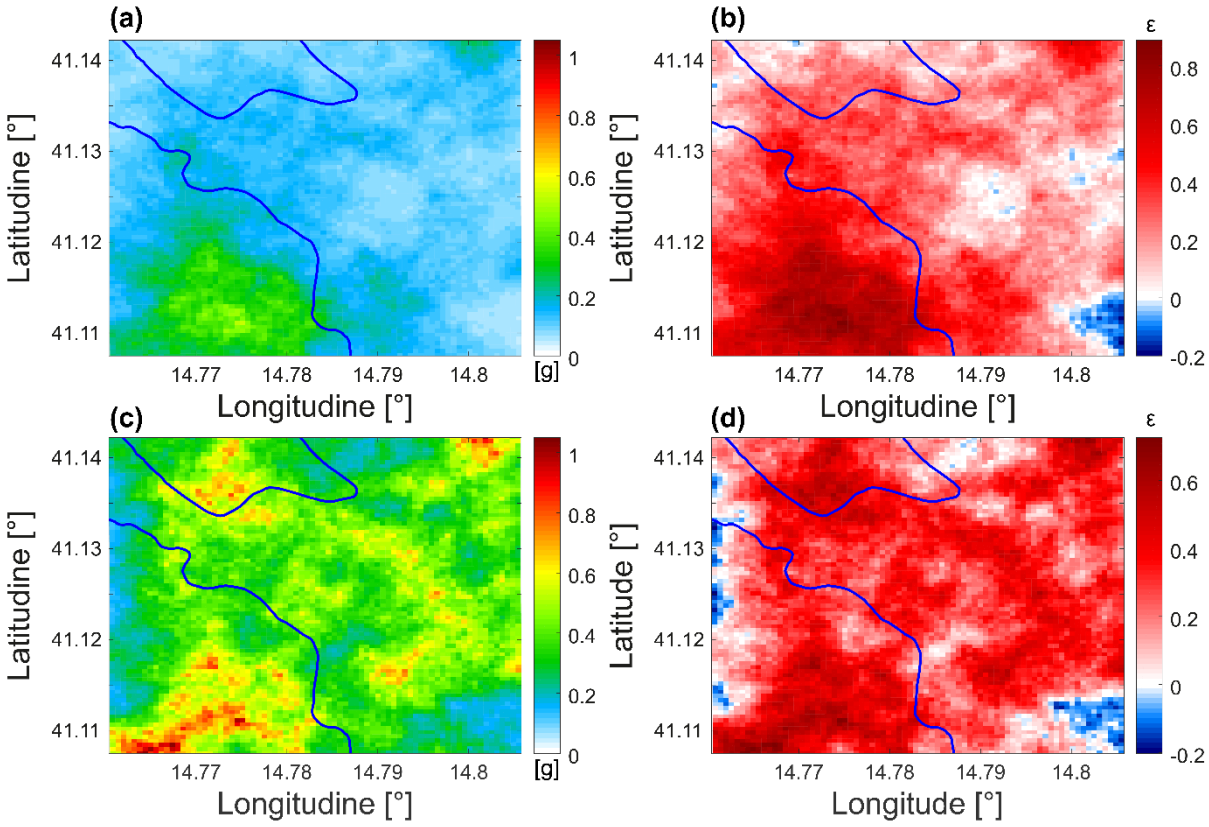

1182

1183 **Fig. 15** Single realizations of shakemaps and corresponding residual maps for (a,b) PGA and

1184 (c,d) Sa(T=0.2s).

1185

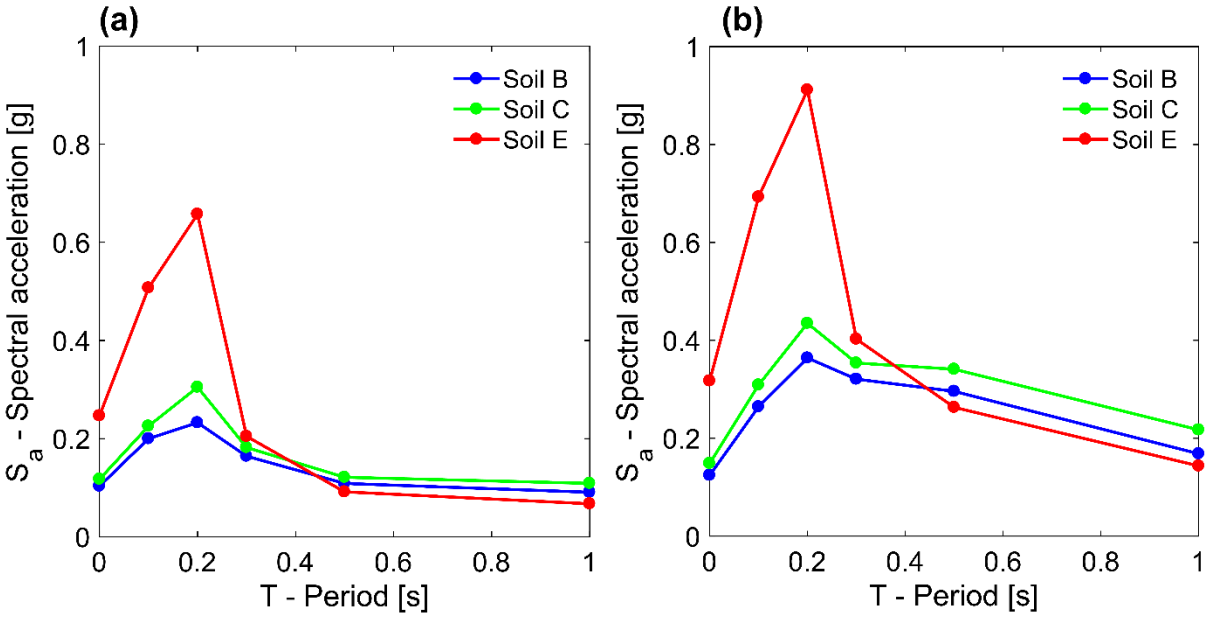

Fig. 16 (a) Single simulation of multiple intensity measures for three grid cells characterized by soil B, C, and E. (b) Average of 10.000 simulations of multiple intensity measures for the same three grid cells of (a).

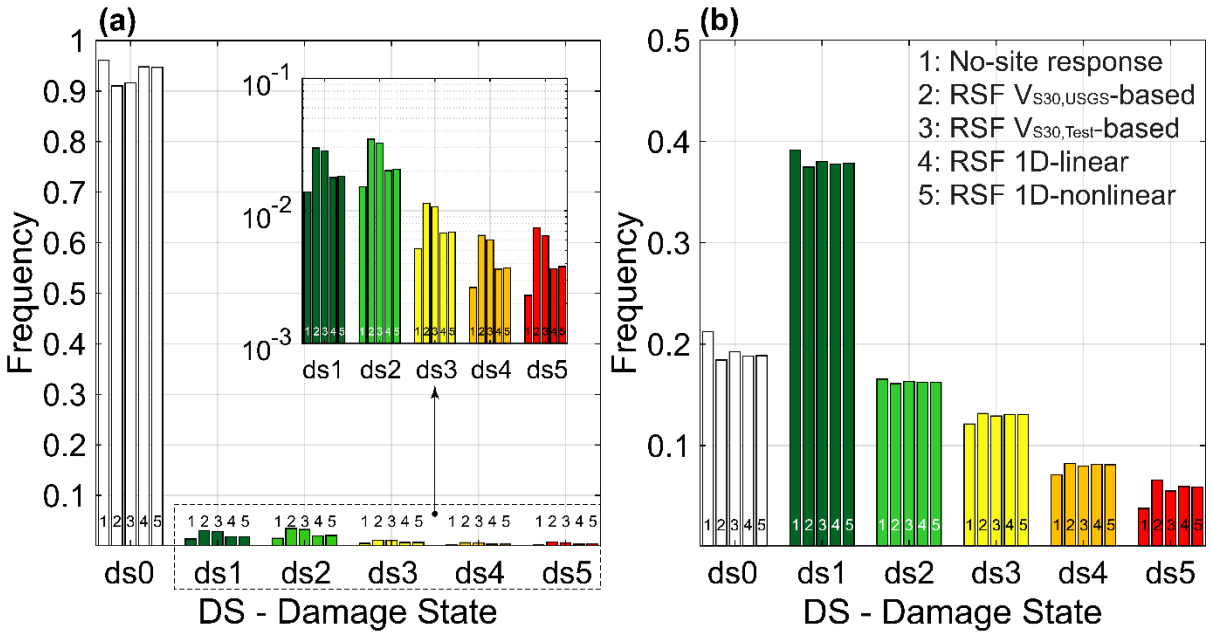

Fig. 17 Frequency of damage states observed over the 10,000 simulations for the five cases of site response analysis for (a) reinforced concrete buildings and (b) masonry buildings.

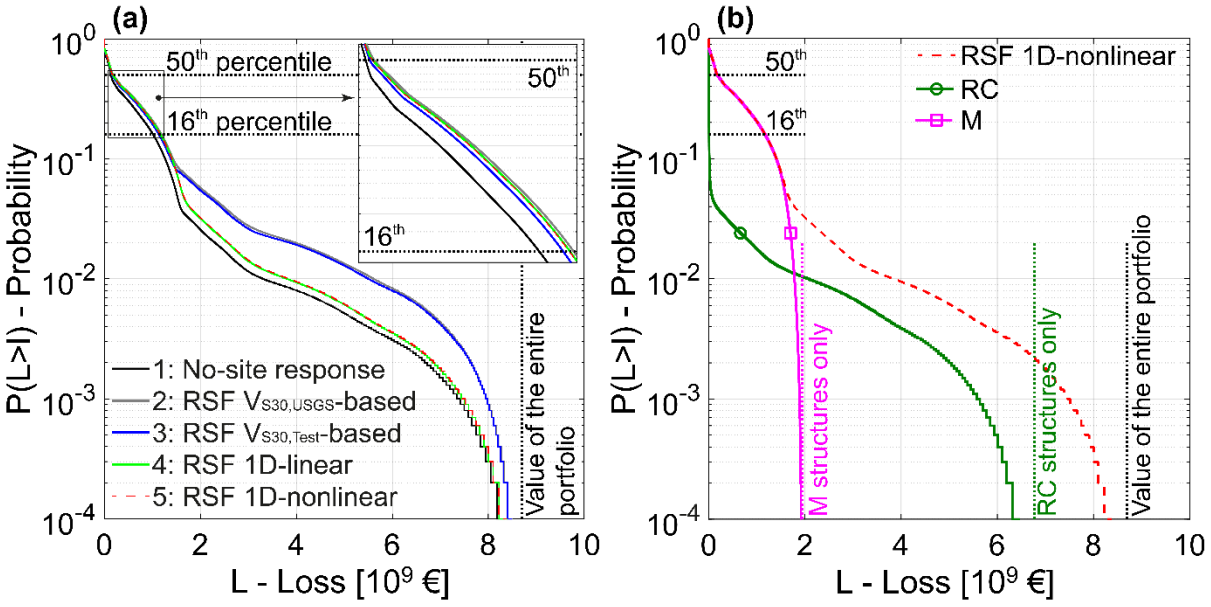

Fig. 18 (a) Loss curves for the five cases of site response analysis. (b) De-aggregation of the losses computed considering the non-linear mono-dimensional propagation for masonry (M) and reinforced concrete (RC) structures.

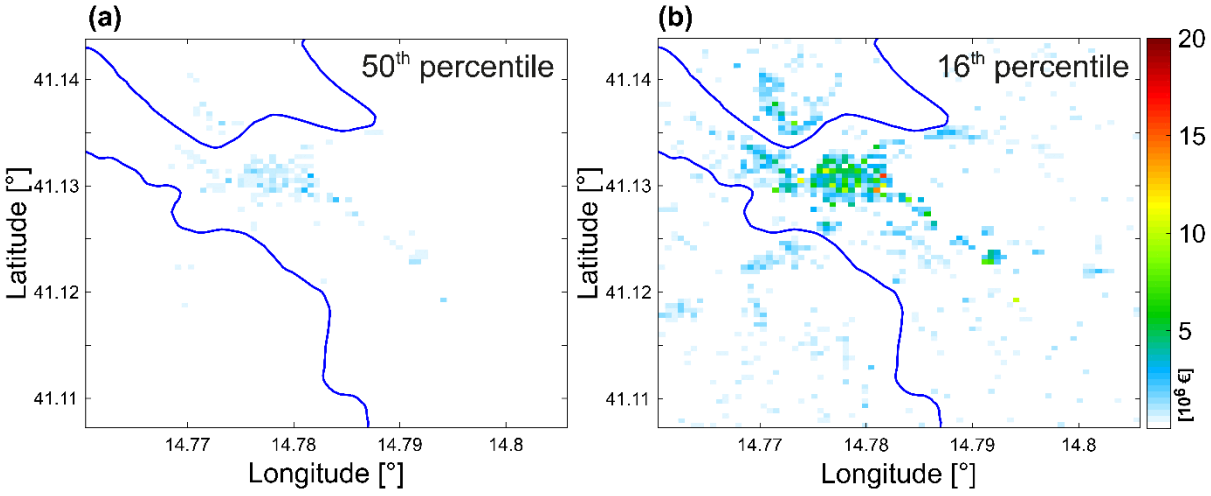

Fig. 19 Risk maps obtained considering the non-linear mono-dimensional propagation, corresponding to the (a) 50th percentile and to the (b) 16th percentile of the loss curve.

Tables

Table 1 Mechanical properties of soils for the non-linear modelling.

ID	Description	ξ_0 [%]	C	R
R	Man-made ground	5.0	436,407	2.38
CL	Fine debris colluvium	3.0	552,591	2.54
DT	Coarse debris colluvium	2.5	12,990,307	3.03
ALG	Recent alluvium	2.0	436,407	2.38
GS	Terraced alluvium	1.0	167,956	2.38
FLF	Fine fluvial lacustrine	5.0	475,33	2.38
FLG	Coarse fluvial lacustrine	1.0	167,956	2.38
CR-ALT	Weathered Rissian conglomerate	1.0	10,308	2.09
CR	Cemented Rissian conglomerate	0.5	7,041	2.38
AGA-ALT	Shallow Pliocene clay	3.0	170,899	2.59
AGA	Deep Pliocene clay	2.0	170,899	2.59
SAP-ALT	Weathered Pliocene sandstone	1.0	10,308	2.09
SAP	Cemented Pliocene sandstone	0.5	18,294	2.38
AV-ALT	Shallow varicolored clay	4.0	47,533	2.38
AV	Deep varicolored clay	3.0	47,533	2.38

Table 2 Real estate values for the case study.

[€/m^2]		Residential	Commercial	Productive	Tertiary
B1	Min	1,275	1,800	1,400	1,600
	Max	1,550	3,000	2,600	2,100
B2	Min	1,398	1,417	1,300	1,650
	Max	1,790	1,967	1,700	2,050
C1	Min	1,182	1,280	553	1,450
	Max	1,420	1,767	775	1,850
C2	Min	958	890	438	800
	Max	1,145	1,193	718	1,000
D1	Min	941	1,200	320	1,125
	Max	1,156	1,500	465	1,425